

29

NPS-61-89-014

# NAVAL POSTGRADUATE SCHOOL

## Monterey, California

AD-A214 013



DTIC  
SELECTE  
NOV 01 1989  
S E D  
C

CHARGING CHARACTERISTICS OF DYNAMICS EXPLORER 1  
RETARDING ION MASS SPECTROMETER  
AND  
THE CONSEQUENCE FOR CORE PLASMA MEASUREMENTS

R. C. OLSEN

SEPTEMBER 1989

Technical Report

Approved for public release; distribution unlimited.

Prepared for:  
Naval Postgraduate School, Monterey, CA 93943-5000 and  
NASA Marshall Space Flight Center, Huntsville, AL 35812

85 10 30 162

Naval Postgraduate School  
Monterey, California


Rear Admiral R. W. West, Jr.  
Superintendent

H. Shull  
Provost

The work reported herein was supported in part by the Naval Postgraduate School and the NASA Marshall Space Flight Center.

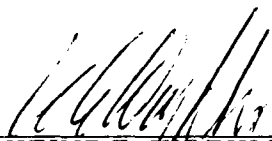
Reproduction of all or part of this report is authorized.

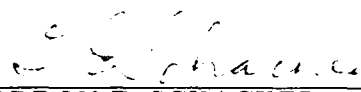
This report was prepared by:

  
R. CHRISTOPHER OLSEN  
Associate Professor of Physics

Reviewed by:

Released by:

  
KARLHEINZ E. WOEHLE  
Chairman, Department of Physics

  
GORDON E. SCHACHER  
Dean of Science and Engineering

REPORT DOCUMENTATION PAGE

1a. REPORT SECURITY CLASSIFICATION unclassified		1b. RESTRICTIVE MARKINGS	
2a. SECURITY CLASSIFICATION AUTHORITY		3. DISTRIBUTION/AVAILABILITY OF REPORT Approved for public release; distribution unlimited	
2b. DECLASSIFICATION/DOWNGRADING SCHEDULE			
4. PERFORMING ORGANIZATION REPORT NUMBER(S) NPS-61-89-014		5. MONITORING ORGANIZATION REPORT NUMBER(S)	
6a. NAME OF PERFORMING ORGANIZATION Naval Postgraduate School	6b. OFFICE SYMBOL (if applicable) 61	7a. NAME OF MONITORING ORGANIZATION	
6c. ADDRESS (City, State, and ZIP Code) Naval Postgraduate School Physics Department (Code 61) Monterey, CA 93943-5000		7b. ADDRESS (City, State, and ZIP Code)	
8a. NAME OF FUNDING SPONSORING ORGANIZATION NASA Marshall Space Flight Ctr.	8b. OFFICE SYMBOL (if applicable)	9. PROCUREMENT INSTRUMENT IDENTIFICATION NUMBER NASA-N 622719RWE90060 O&MN, Direct Funding	
8c. ADDRESS (City, State, and ZIP Code) Huntsville, AL Naval Postgraduate School (Code 61) Monterey, CA 93943-5000		10. SOURCE OF FUNDING NUMBERS	
		PROGRAM ELEMENT NO.	PROJECT NO.
		TASK NO.	WORK UNIT ACCESSION NO.
11. TITLE (Include Security Classification) Charging Characteristics of Dynamics Explorer I Retarding Mass Spectrometer and the Consequence for Core Plasma Measurements			
12. PERSONAL AUTHOR(S) R. C. Olsen			
13a. TYPE OF REPORT Technical	13b. TIME COVERED FROM Sep 89 TO Sep 89	14. DATE OF REPORT (Year, Month, Day) 890914	15. PAGE COUNT 51
16. SUPPLEMENTARY NOTES			
17. COSAT CODES		18. SUBJECT TERMS (Continue on reverse if necessary and identify by block number)	
FIELD	GROUP	SUB-GROUP	
		Spacecraft charging; thermal plasmas; mass spectrometry.	
19. ABSTRACT (Continue on reverse if necessary and identify by block number) The Retarding Ion Mass Spectrometer (RIMS) on the Dynamics Explorer I (DE I) satellite has provided a new range of data, and challenges for studies of the core plasma of the magnetosphere. Analysis of the RIMS data provides a measure of the satellite potential in the inner magnetosphere. As the satellite leaves the inner plasmasphere, it begins to charge positively, crossing the 0 V mark at about 1000 cm <sup>-3</sup> . The potential rises slowly initially, reaching about 1 V near the plasmopause, at the 100 cm <sup>-3</sup> point. At lower densities, the potential rises relatively rapidly, reaching +5 V or greater at the 10 cm <sup>-3</sup> point. For satellite potentials of +1 to +5 V, portions of the ion distribution function are lost to measurement because the ions are repelled by the satellite. In particular, in a multi-temperature plasma, the cold component is easily lost in this potential (density) regime. It is in this regime where aperture bias techniques have been successfully used, particularly in measurements of field-aligned ion flows such as the polar wind, which have sufficient kinetic energy to overcome electrostatic barriers in front of the aperture plane. At lower densities (<10 cm <sup>-3</sup> ), the satellite potential can exceed +5 V. At such potentials the core plasma is lost to the RIMS, and even the aperture bias techniques are no longer successful.			
20. DISTRIBUTION STATEMENT OF ABSTRACT <input checked="" type="checkbox"/> UNCLASSIFIED UNLIMITED <input type="checkbox"/> SAME AS RPT <input type="checkbox"/> DTIC USERS		21. ABSTRACT SECURITY CLASSIFICATION unclassified	
22a. NAME OF RESPONSIBLE INDIVIDUAL Professor R. C. Olsen		22b. TELEPHONE (Include Area Code) 646-2019	22c. OFFICE SYMBOL 610s

CHARGING CHARACTERISTICS OF DYNAMICS EXPLORER 1  
 RETARDING ION MASS SPECTROMETER  
 AND  
 THE CONSEQUENCE FOR CORE PLASMA MEASUREMENTS

R. C. Olsen  
 Physics Department  
 Naval Postgraduate School



1 August 1989

Accession For	
NTIS GRA&I	<input checked="" type="checkbox"/>
DTIC TAB	<input type="checkbox"/>
Unannounced	<input type="checkbox"/>
Justification	
By _____	
Distribution/	
Availability Codes	
Avail and/or	
Dist	Special
A-1	

## SUMMARY

The Retarding Ion Mass Spectrometer (RIMS) on the Dynamics Explorer 1 (DE 1) satellite has provided a new range of data, and challenges for studies of the core plasma of the magnetosphere. Analysis of the RIMS data provides a measure of the satellite potential in the inner magnetosphere. As the satellite leaves the inner plasmasphere, it begins to charge positively, crossing the 0 V mark at about  $1000 \text{ cm}^{-3}$ . The potential rises slowly initially, reaching about 1 V near the plasmopause, at the  $100 \text{ cm}^{-3}$  point. At lower densities, the potential rises relatively rapidly, reaching +5 V or greater at the  $10 \text{ cm}^{-3}$  point. For satellite potentials of +1 to +5 V, portions of the ion distribution function are lost to measurement because the ions are repelled by the satellite. In particular, in a multi-temperature plasma, the cold component is easily lost in this potential (density) regime. It is in this regime where aperture bias techniques have been successfully used, particularly in measurements of field-aligned ion flows such as the polar wind, which have sufficient kinetic energy to overcome electrostatic barriers in front of the aperture plane. At lower densities ( $<10 \text{ cm}^{-3}$ ), the satellite potential can exceed +5 V. At such potentials, the core plasma is lost to the RIMS, and even the aperture bias techniques are no longer successful.

## I. INTRODUCTION

The thermal plasma measurements on Dynamics Explorer 1 (DE 1), using the Retarding Ion Mass Spectrometer (RIMS) have provided a new look at the satellite density-potential relationships for the inner magnetosphere. Previous publications on the effect of satellite charging on the RIMS measurements (Olsen et al., 1985b, 1986) have considered the effect of illumination on measurements near local midnight, in equatorial regions, and the effectiveness of aperture plane bias experiments. Other reports have considered the effect of satellite potential on the inference of basic plasma parameters in the plasmasphere (Comfort et al., 1985), and the consequences of various instrument anomalies on the core plasma measurements (Olsen et al., 1985a).

In this presentation, the plasmasphere data will be summarized in terms of the density-potential relationship, illustrating the regime where RIMS accurately measures the core plasma. This relationship is then compared to a similar relation established for GEOS, at lower densities (higher potentials). The base of plasmasphere measurements will then be extended into the plasmopause region ( $10 \text{ cm}^{-3} < n < 100 \text{ cm}^{-3}$ ), at low and high latitudes. This region will be considered from a viewpoint of varying illumination (i.e. eclipse), and aperture plane potential control, and a combination of the two, for a few unique examples. Finally, the regions outside the plasmasphere are considered, where there are apparently times when RIMS is prevented from observing the core plasma by satellite potential greater than the thermal or flow energy of the ambient plasma. It is our purpose to use the DE 1 experience to give an indication of what spacecraft charging effects can be anticipated in other spacecraft whose purpose is to measure magnetospheric plasma properties.

## II. PLASMASPHERE DENSITY-POTENTIAL RELATION

A fundamental element in understanding and analyzing charged particle data is the satellite potential-density relation. If known, such a relationship can be used to aid in analysis, and can be used to predict instrument response. The substantial data set obtained in the analysis of the RIMS plasmasphere data (Comfort et al., 1985) enable us to begin the determination of the relationship between the ambient plasma density and detector potential, as illustrated by Figure 1. This figure was obtained by a straightforward sort of all available plasmasphere passes for the fall 1981 RIMS data (data processed as of mid-1986). The data were split into dayside (800 LT) and nightside (1800 LT) segments, initially for convenience, and then as it became clear that there were significant differences in the results for the two local time sets, as discussed below. The axes for Figure 1 are chosen to match a similar figure constructed for GEOS, as presented below. The physical relationship between plasma density and detector potential we expect to find suggests such a choice. In particular, the emitted photocurrent, one of the major terms in the satellite current balance, will vary as  $\exp(-e\phi/kT)$ , for positive satellite potentials. At the same time, the attracted ambient electron current will vary in a primarily linear way with ambient electron density. The relative importance of these two effects is illustrated by the data points above the  $\phi > 0$  mark, in Figure 1. In this region there is a nearly linear relationship between the log of the density and the detector potential. For high densities (negative potentials), the relationship changes. The balance is then between the ambient electron current, and the ambient ion current (enhanced by ram, or satellite velocity effects). There is a hysteresis in the curve between  $-0.5$  and  $0.0$  V satellite potential, which has been attributed to satellite velocity effects.

These data can be compared to the density potential relation obtained on GEOS. On GEOS 1 and 2, the satellite potential, as inferred from the electric field experiment, was compared to the total electron density, as measured by the plasma wave experiments. The

electric field experiment obtains a measure of the satellite potential by operating the spherical probes as Langmuir probes. The probes are biased to close to the plasma potential by forcing a negative current into the spheres. Figure 2 presents the results published by Knott et al., (1983) and Schmidt and Pederson, (1987) with the DE1/RIMS results overlaid. The RIMS data points are plotted as dots, for densities over  $100 \text{ cm}^{-3}$ . The last six data points, extending to lower density, are connected with solid lines to insure their visibility. The stars and dots below  $100 \text{ cm}^{-3}$  are the GEOS data points.

The lines in the lower sections are from fits to the data (solid line, long dashed line), while the short dashed line is from a model which incorporated ambient electrons, photoelectrons, and a spherical satellite model. Ambient electron temperatures of 0.5, 1.5 and 4.0 eV were used by Knott et al., (1983), but only the 0.5 eV curve is shown in this figure. Fits to the data using an expected functional relationship between  $\log(\text{density})$  and potential give:

$$\log(\text{density}) = 3.555 - 1.318 \phi^{0.42}$$

or, inverting

$$\phi = 14.1 - 9.26 [\log(n)]^{0.46}$$

with potential ( $\phi$ ) in volts, and density ( $n$ ) in  $\text{cm}^{-3}$ .

Note that Knott's model approaches the best fit quite closely when this data set is used. Agreement is better than that initially obtained by Knott et al., (1983), with a more limited data set. (Note, the labels in Figure 2 duplicate those in the original figure, including an apparent error in the Knott et al. reference.)

This density-potential relation can be used to aid in the analysis of RIMS data, particularly data taken after the failure of the radial RPA. This has been done, with results under preparation in a variety of efforts (R. H. Comfort, private communication, 1989). Also we can consider the implications of these results for RIMS measurements at



densities below  $1000 \text{ cm}^{-3}$  for model environments. First, let us consider measurements of the low temperature, isotropic, core plasma. The analysis makes use of a model developed for RIMS processing by Comfort et al. [1985]. The thin sheath (TSHEATH) algorithm for a limited aperture RPA was applied by manually incorporating the density-potential relationship illustrated in Figure 2. This algorithm makes it possible to simulate the detector response. Addressing isotropic plasmas first, an ensemble of curves is found as shown in Figures 3a and 3b. It was assumed that the satellite was moving at 3 km/s with respect to the plasma, and that the hydrogen ions had a characteristic temperature of 1.0 eV. For the end head (Z), it was assumed that the flow was perpendicular to the aperture plane normal. For the radial detector (R), simulated spin curves were created, assuming 0 V settings for the RPA. Simulations of the end head (Z) RPA response (Figure 3a) show that the core plasma is visible at densities down to  $10 \text{ cm}^{-3}$  ( $\phi_s/c = 5\text{V}$ ) at which point the count rate drops below 1 count/accumulation. (The flux drops with temperature; the end head response is less than 1 count/accumulation at  $25 \text{ cm}^{-3}$  for 0.5 eV, or  $70 \text{ cm}^{-3}$  for 0.1 eV). In principle, it is possible to sum over long time periods, thus resolving any sensitivity problems. This has been done for some RIMS data, particularly over the polar cap (Nagai et al., 1984). Often, however, there is a warm ( $T \geq 5 \text{ eV}$ ) plasma which will produce a 1-10 count/accumulation background, obscuring the core plasma. (For example, at  $1 \text{ cm}^{-3}$ , 10 eV, RIMS will show a count rate of 10 counts/accumulation).

Simulations of the radial detector spin response to the same plasma/spacecraft potential combinations are shown in Figure 3b, where a 3 km/s satellite velocity is assumed (near apogee). Spin curve analysis can again produce useful results at densities down to  $10 \text{ cm}^{-3}$ . This result is affected by the satellite velocity and plasma temperature. For example, a warm plasma ( $T = 1 \text{ eV}$ ) is easier to measure than a cool plasma ( $T = 0.5 \text{ eV}$ ), at a given velocity.

The radial detector response as a function of plasma density and temperature is summarized for three representative satellite velocities (altitudes) in Figures 4abc. If we

again take the criteria that the plasma is "measurable" at the 1 count level, these curves then provide the cutoff density which can be measured as a function of temperature. Characteristic temperatures for 0.1, 0.33, 0.5, and 1.0 eV were chosen. These are characteristic of the ionosphere, inner plasmasphere, outer plasmasphere/plasmapause, and outside the plasmasphere, respectively. Not all of the combinations are physically meaningful, of course. It is unlikely that an 'ionospheric' plasma of  $500 \text{ cm}^{-3}$  density and 0.1 eV temperature will occur at apogee. These parameters help to indicate the general trend, however. As the temperature increases, the necessary plasma density decreases. The results of the apogee model are supported by the work of Olsen et. al. [1985, b], and are further illustrated later in this report.

### III. POLAR WIND SIMULATION

One of the major concerns of the RIMS scientists has been the ability of RIMS to adequately measure the polar wind. This was done, as reported by Sojka et al., (1983) and Nagai et al., (1984), and illustrated later in this document. At this point, we consider the implications of the density-potential relation developed in the previous section for polar wind measurements. The term polar wind, is used here to mean cold plasma moving upward due to ambipolar diffusion (Banks & Holzer, 1968). Typical initial velocities are a few km/s. Such upward flows interact with the local fields, and can gain energy. This energization process makes it difficult to predict the velocity, so a full range of density-velocity parameters must be considered. Fortunately, flux conservation makes it possible to restrict the combinations of density and velocity. The polar wind simulation was done assuming the escape flux is constant at  $2 \times 10^8 \text{ ions/cm}^2 \text{ s}$ , the classical low altitude value. It was assumed that the polar wind was escaping into a vacuum (i.e. no background plasma), and expanding in area as  $1/B$  (i.e. flux  $\propto 1/R^3$ ). The collapse of the solid angle filled by the distribution was ignored. The unknown flow velocity then depends

inversely on density. The result for the plasma parameters previously chosen ( $n = 7$  to  $700 \text{ cm}^{-3}$ ) at low altitudes was that at all but the highest density, the flow velocity was so high (greater than  $20 \text{ km/s}$ ) that: a) the thin sheath algorithm failed because of the high Mach number; and b) it became clear that with the high flow energy (e.g.  $4 \text{ eV}$  for  $28 \text{ km/s}$ ) there was no way the polar wind would remain "hidden" for the lower densities (see Table 1). These results are not really surprising. Analysis of the low altitude data (below  $3000 \text{ km}$ ), has been proceeding, and typical values of  $2\text{--}20 \text{ km/s}$  are being found (M. O. Chandler, private communication, 1987).

Table 1                      Polar Wind Flow Energy -                       $2 \times 10^8 \text{ ions/cm}^2 \text{ s}$

n	flow velocity	flow energy
$700(\text{cm}^{-3})$	2.86 km/s	0.04 eV
70	28.6 km/s	4.3 eV
25	80 km/s	33. eV
15	133 km/s	91. eV
9	222 km/s	257. eV
7	286 km/s	425. eV

Extending the model upward shows that as long as satellite velocity effects are included, the plasma remains measurable up to about 1 RE altitude, so long as the temperature is allowed to increase slightly. Above this altitude, the polar wind begins to fade from view. Figure 5 shows the count rate expected for RIMS, as a function of density (velocity) and temperature, at 4 altitudes. An escape flux of  $2 \times 10^8 \text{ ions/cm}^2 \text{ s}$  (e.g. winter) is assumed at  $100 \text{ km}$ . The count rate is then considered at distances of 1, 2, 3, and 4 RE along the magnetic field line, roughly corresponding to satellite altitudes of similar magnitude. The  $L = 6.6$  field line was used, and the 4 RE panel corresponds to satellite apogee. The first set of values, at 1 RE, show that the polar wind may be missed if it does not 'warm up' to  $0.2 \text{ eV}$ . At 2 RE altitude, the flux has dropped by a factor of 30 relative to the  $100 \text{ km}$  value. As a result, a substantial range of likely polar wind values are unmeasurable. The

polar wind would be measurable only if it remained subsonic, or became highly supersonic. At higher altitudes, the polar wind flux would only be measurable if the flow velocity dropped to a few hundred meters per second, e.g. the flow largely ceased. The ions would then effectively form a stationary plasmasphere population from the RIMS perspective.

One caveat here is the pitch angle distribution. Ignoring the effect of electric fields, etc., there would be a pitch angle folding which would restrict the angular distribution, giving for example, at 3 RE an upper limit of about 20 degrees to the pitch angle distribution. The focusing of particles into a narrow angular cone would give the ion distribution function a unique signature which would allow 'polar wind' to be separated from the isotropic plasmasphere.

Variations in the ionosphere escape flux from the canonical value by a factor of 2 lead to relatively small changes in the results illustrated by Figure 5. The effect of varying the flux around the expected (winter) values are shown in the top two panels of Figure 6. For example, at 3 RE, an increase in flux of a factor of 2 brings the highly supersonic solutions ( $1 \text{ cm}^{-3}$ , 60 km/s) into view at all temperatures, but results in no other major changes. Reducing the flux by a factor of 2 has little effect on the subsonic solutions, and causes the  $1 \text{ cm}^{-3}$  measurements to drop out. The behavior at high density/low velocity is a result of the dominance of satellite velocity. Polar wind fluxes an order of magnitude lower (e.g. summer,  $1-2 \times 10^7 \text{ ions/cm}^2 \text{ s}$ ), will remain observable at high density/low flow velocity, following the pattern seen in the lower right hand panel of Figure 6. Supersonic polar wind would not be observable. (The  $1 \text{ cm}^{-3}$ , 25 km/s solutions also give less than 1 count.)

The addition of a background plasma to the model allows for reduced potentials. This is illustrated in the lower left panel of Figure 6. At 3 RE, a  $70 \text{ cm}^{-3}$  background holds the potential to +2 V or less, and the polar wind becomes visible if its temperature is above 0.2 eV. This is consistent with the results of Nagai et al. (1984). It was found that the polar wind was visible, without aperture bias techniques, at a level of 20-25 counts/accumulation. These observations were made at a time when the background was

between 50 and 100  $\text{cm}^{-3}$  (Gallagher et al., 1986). This latter condition was apparently unusual in the DE-1 data set, and was the result of a major magnetic storm. Further searches of the DE 1/RIMS data set for high altitude ( $> 1 \text{ RE}$ ) polar wind observations have largely proven unsuccessful, even using aperture bias techniques, which can balance out some of the satellite charging effects. It now appears that the uniqueness of the observations reported by Nagai et al., lie in the nature of the background plasma on that day, and not the nature of the polar wind.

The energized, heated, and scattered beams which form at low densities have been reported at geosynchronous orbit by Olsen (1982) and for ISEE-1 out to  $L=11$  by Nagai et al. (1983). Some aspects of the above modeling presumably break down at this point. Still, it appears that we can conclude that there is an intermediate region spatially, and energetically, where the field aligned ions of the polar wind are not observed. The ions can be observed at the beginning of their upward trajectory, and at the end, but the intermediate region remains obscured.

#### IV. ECLIPSE DATA

One of the most useful clues in ferreting out charging effects on core plasma data is provided by satellite passages through eclipse. By cutting off the large photocurrent normally caused by sunlight, the satellite is allowed to reach a less positive potential. In the inner plasmasphere, the effect is small, perhaps a tenth of a volt shift. In the outer plasmasphere, however, significant shifts are possible, up to several volts, resulting in potentials near zero volts. Analysis of the Spring, 1982 eclipse data available in 1983 and 1984 resulted in one publication on this topic (Olsen et al., 1985a). Further analysis of the data, as they arrived, supported the original conclusions. These are: that the isotropic  $\text{H}^+$  is successfully measured by RIMS in sunlight and shadow, so long as the density is greater than  $30 \text{ cm}^{-3}$ . At some point below this, the cold component is lost, not entirely because

of sensitivity problems, but because the tail of the core distribution is covered by the increasingly important supra-thermal population. The He+ component of the core plasma is lost at the same time, primarily for reasons of sensitivity. When O+ is present, it is relatively easy to measure, because the satellite ram velocity focuses the ion flux into a relatively small solid angle, and the O+ has nearly an eV of kinetic energy for typical satellite velocities.

Two examples are given of the behavior of isotropic core plasma measurements at the eclipse transition. Figure 7 is from day 47 of 1982. The instrument is in mass scan mode, so only spin curves are available. Hydrogen and He+ are sampled along with N++/O++, and molecular ions. Only the two light ions are observed at this time. The satellite enters eclipse while in the plasmasphere,  $L = 3.55$ ,  $-4^\circ$  magnetic latitude,  $n = 450 \text{ cm}^{-3}$  (PWI). The core plasma is clearly visible in both sunlight and eclipse at eclipse entry. At eclipse exit (2325 UT,  $L = 4.9$ ,  $20^\circ$  magnetic latitude,  $n = 75 \text{ cm}^{-3}$  (PWI)) a different behavior is found - the plasma disappears.

Figure 8 shows data from day 65 of 1982. The radial detector low mass channel (H+) spin curves are not available, due to channeltron degradation, but end head RPA data are available. The core plasma is visible in sunlight and eclipse at eclipse entry (0754 UT,  $L = 3.3$ ,  $-3^\circ$  magnetic latitude,  $n = 376 \text{ cm}^{-3}$ ). At eclipse exit, however, the plasma disappears from view in sunlight (0911 UT,  $L = 5.1$ ,  $21^\circ$  magnetic latitude,  $n = 70 \text{ cm}^{-3}$ ).

The previous examples illustrated the behavior of isotropic plasma at eclipse transitions. Extensive processing of the eclipse "exit" data will generally show the isotropic flux at a low count level, but these figures illustrate the basic point - the plasma fades from view. Anisotropic plasma, primarily field-aligned in the present context, follows the above patterns. The field-aligned distributions may persist past the eclipse exit, or may disappear as the satellite potential increases. Figure 9 illustrates the former case. Data from Day 46 of 1982 show H+ data from the -Z detector, for RPA analysis, and the radial detector, for pitch angle distribution. The warm, mainly isotropic

background fades at eclipse exit (1957 UT), but the field-aligned distribution persists. (Density is  $5-10 \text{ cm}^{-3}$ ). This is one of two such (clear) cases found in Spring 1982. By contrast, 4 cases were found where the field-aligned ions disappear at eclipse exit, as illustrated in Olsen et al., (1985b), plate 3. The major significance of these data are (a) they demonstrate the existence of "hidden" plasmas, and (b) they show the importance of taking data in eclipse.

## V. APERTURE PLANE POTENTIAL CONTROL

Previous publications concerning the effectiveness of aperture plane potential control for RIMS (Chappell, et al., 1982. Olsen et al., 1986, Nagai et al., 1984; Sojka et al., 1983) have focused on relatively narrow regions, particularly the polar cap/polar wind region. In this section, a synoptic view is given of the effect of the aperture plane (day 287), and then for a number of days in the following years.

The orbit of the satellite for day 287 of 1981 is shown in Figure 10. Figure 11 shows spin-time spectrograms for  $\text{H}^+$  for aperture plane settings of a) 0V, b) -2 V, c) -4 V, and d) -8 V. Figure 12 illustrates the spin-time spectrograms for  $\text{He}^+$  at the 4 bias settings, and Figure 13 the corresponding  $\text{H}^+$  RPA-time spectrograms for the radial detector. Beginning on the left hand side of these latter 3 figures, (hour 20-21 UT), the satellite is in the night side polar cap. The "classical" polar wind is visible here, as the field aligned flux is visible at all bias settings. At -8 V bias, an otherwise invisible isotropic component appears. This plasma, combined with an oxygen component inferred from measurements by the High Altitude Plasma Instrument (HAPI), comprise an unusually high plasma density for the polar cap, and has been the topic of articles by Gallagher et al., (1986), and Menietti et al., (1985). The satellite then enters the plasmasphere, where the detector saturates at non-zero aperture plane settings. When the

satellite leaves the plasmasphere, thermal plasma is again visible at all bias settings. At  $-4$  V and  $-8$  V, an additional feature appears that is not apparent at  $0$  V and  $-2$  V. This is a field-aligned ion flux that is otherwise repelled by the satellite potential. This plasma was extensively analyzed by Sojka et al., (1983), and Olsen et al., (1986).

These data were the impetus for continued, and frequent operations of the RIMS with the aperture plane cycling ( $0/-8$ ; or  $0/-2/0/-4/0/-8$ ) or set at  $-8$  V. Unfortunately, it took many more months before these later data became available. Analysis of these data showed that the aperture plane technique had several undesirable features, when used regularly. The primary problem was the frequent, and long-term saturation of the channeltrons, which caused extensive detector degradation. The useful lifetime of the detector was substantially shortened, and much of the 1982 data set was rendered useless by these operational choices. Part of the problem was the independent failure of the radial detector RPA, which meant an associated loss of energy analysis of the plasma, all arriving with relatively high kinetic energy.

The loss of data, particularly plasmasphere data, might have been considered a worthwhile trade-off, if otherwise unmeasured features of the inner magnetosphere could then be observed. Unfortunately, a survey of all 1982 orbits with  $0/-8$  V cycling (for which data is available) (13 orbits) resulted in no observations which indicated such success. Consideration of whole orbits of full cycle data ( $0/-2/0/-4/0/-8$  V) showed a similar result. Whole orbits at  $-8$  V bias were effectively useless.

The basic problem is that the barrier effect (discussed by Olsen et al., 1986) becomes operative very quickly as the satellite potential exceeds a few volts. Briefly, the barrier effect is as follows. For a positive spacecraft, and small negative surface elements, Laplace's equation requires that the local minimum in the potential distribution in one direction (say the azimuthal direction) must be balanced by a local maximum in other directions (say the radial direction). Figure 14 illustrates this point. The local minimum in the horizontal direction (in the plane of the object), is balanced by a local maximum in



the vertical direction. For the core plasma, this means that the satellite potential, or barrier height, exceeds the thermal energy of the plasma.

The operational pattern for the aperture plane was revised when the latter 1982 data arrived. Eventually, in late 1983, the channeltrons recovered in sensitivity, and the satellite orbit entered a phase where useful data could be obtained from the aperture plane experiments. This is the regime where satellite potential is a few volts, e.g. densities from  $10\text{--}100\text{ cm}^{-3}$ . Operation of the aperture plane at  $0\text{--}8\text{ V}$  in the outer plasmasphere, at low altitudes, allowed observations of the isotropic background (particularly He+) which would not otherwise have been possible. An illustration of this is shown in Figure 15, which shows data from 23 October 1983 (day 296). The satellite is near local dusk (20 LT), within  $30\text{--}35$  degrees of the magnetic equator, where heated plasma is often found (Olsen et al., 1987). The addition of  $-8\text{ V}$  bias allows the cold background plasma to be observed. The local minimum in total electron density at the equator ( $n \sim 25\text{ cm}^{-3}$ ) becomes clearly visible in the He+ data, as the He+ flux drops to near zero. (Away from the equator  $n \sim 40\text{ cm}^{-3}$ .)

## VI. CHANNELTRON SATURATION

The channeltron degradation effect is well illustrated by data taken several years after launch. The aperture bias was still being utilized in the  $0\text{--}2/0\text{--}4/0\text{--}8\text{ V}$  mode. Initial modes (e.g. 1982–1983) utilized 1 minute command intervals. The operations staff found this level of effort difficult to maintain, and the sequence intervals were increased to 128 seconds. This allowed short-term degradation and recovery effects to be observed.

Figure 16 shows H+ data from that radial detector during one such sequence in 1986. The satellite is at low latitudes ( $-5^\circ$  to  $-15^\circ$ ), moving from 3.2 to 3.6 RE, near local dawn. The plasma environment (as seen) is largely isotropic. The absolute density is nominally in the  $10\text{--}100\text{ cm}^{-3}$  range, the potential a few volts positive. Data here have been averaged

over 6–8 second intervals, and are essentially spin averaged. At  $-8$  V bias, the detector saturates, resulting in near zero counts, as seen at 0909 UT. The detector recovers when the bias reverts to 0 V, with a time constant of about one minute, as seen at 0900, and 0912. The  $-4$  V setting results in less serious degradation, but the count rate drops by at least one order of magnitude as seen at 0905. The  $-2$  V setting does not saturate the detector (0901, 0914), so there is no decay, or associated recovery at the subsequent 0 V setting. The helium data behave in a similar way, but are better illustrated by a separate series of observations.

Figure 17 shows the  $\text{He}^+$  data taken from the low and high mass channels, for day 105 of 1986. The satellite moves from  $L=4$  to  $L=5$  during this early morning (0900 LT) pass. The  $\text{H}^+$  data are similar to those shown before, but muddled by variations in the pitch angle variation during the period of interest. The  $\text{He}^+$  remains largely isotropic. RIMS operates in modes which allow toggling between  $\text{H}^+/\text{He}^+$  and  $\text{He}^+/\text{O}^+$  measurements on an 8-s cycle. The high mass channel is largely unperturbed by the aperture bias. vis-a-vis degradation. Hence, it represents a control for the low mass channel ("+" signs). The low mass hydrogen flux presumably causes saturation at  $-4$  and  $-8$  V bias, which persists through the next 8-second toggle to the alternate mass settings. Hence, the low mass channel  $\text{He}^+$  decays over the 128-s period. Recovery at 0V is not apparent due to the exclusion of thermal  $\text{He}^+$  from the positive detector.

These illustrations indicate substantial short-term decay/recovery processes occur within RIMS which differ from those traditionally associated with channeltrons. It is not clear what the physical mechanisms are.

## VII. NEGATIVE CHARGING

A major concern from previous satellite missions was the occurrence of large negative charging in the plasma sheet, or auroral regions. Such potentials have been observed in

daylight, at geosynchronous orbit, on ATS-5 (to -300V) and ATS-6 (to -1500V) (Olsen, 1987). At high latitudes, there are reports of momentary (1-100 seconds) negative charging from the DMSP satellites, in shadow, to the level of a few hundred volts (Gussenhoven et al., 1985). At geosynchronous orbit ( $L = 6.6$ ), negative potentials of 1-20 kV are routinely found in eclipse (Olsen and Purvis, 1983; Olsen, 1987). Our present understanding of satellite charging suggests that for DE-1, the satellite should charge negatively if:

a) In eclipse, the satellite is in the plasma sheet, with  $T_e > 6$  KeV, and the Alfvén boundary has  $E > 15$  KeV. These criteria will rarely be met, since the latter is appropriate to  $L \sim 6.6$ , while the satellite is in eclipse at  $L = 2$  to 5.

b) In sunlight, major portions of the satellite are shadowed for tens of seconds, in the plasma sheet. For the DE-1 attitude and orbit, these conditions will only be met when the satellite is at local dawn or dusk. Only the former is a region (typically) of hot plasma, and DE-1 does not normally reach high latitude, low altitude, at this local time.

c) Intense auroral electron beams are encountered, at high latitudes. Observations during the HAPI lifetime occasionally suggested there might be negative charging under this last condition. Ion distributions were observed which could be interpreted as the result of negative charging, or simply field-aligned beams. The latter interpretation was adopted, and the matter dropped.

RIMS observations in eclipse have not shown evidence of negative charging (-1 to -50V). Potentials of greater magnitude would not produce a characteristic response.

## Summary

The results of this survey of DE/RIMS charging behavior can be summarized by referring to Figure 18. The noon-midnight meridian plane is illustrated in Figure 18, with a modified dipole field shown. A standard set of dipole field lines ( $L = 2$  to 6) were

compressed on the dayside (80%), and stretched on the night side (130%). The regions indicated in the figure are the ionosphere, inner and outer plasmaspheres, plasmopause region, and plasma sheet. Boundaries at  $L = 3, 4,$  and  $5$  are typical. Two types of field-aligned flows are indicated on the figure. The subauroral, refilling flows (Decreau et al., 1986) are distinguished here from 'polar wind', which is taken to be a flow onto largely empty field lines at higher latitudes. The higher energy flows on auroral field lines are omitted from consideration.

Beginning with the ionosphere, typical satellite potentials are low (less than 1 V), and the bulk of the cold, isotropic "core" plasma is visible. Moving outward at low latitudes, the inner plasmasphere, with densities greater than  $700 \text{ cm}^{-3}$ , provides an environment which allows satellite potentials from 0 to +1 V. Again, the core plasma is easily observable. Outside this region, in the outer plasmasphere, plasma densities from  $70\text{--}700 \text{ cm}^{-3}$  are typically found, and satellite potentials from +1 to +2 V. The plasma distribution remains measurable throughout this region, but elements of the distribution function can be lost. This is not generally a problem in this region though distortions in particle trajectories may distort subtle vector and tensor properties (flow, heat flux).

In the plasmopause region, densities from  $7$  to  $70 \text{ cm}^{-3}$  are typically found, and satellite potentials from 2 to 5 V are the norm. It is in this region that the isotropic, core plasma becomes hidden. This is due to both detector sensitivity questions, and the development of higher temperature plasma components which obscure the cold plasma. The core plasma is observed at local midnight during satellite eclipse passages. Field-aligned flows (refilling) are generally observed in this region. By definition, the observed flows are energetic enough to overcome satellite potential effects — e.g. flow velocities are tens of kilometers per second. Lower energy flows are of course possible, and

indeed likely. The limited eclipse data set is not conclusive on this point, but it appears that lower energy H<sup>+</sup> flows are being missed in the outer plasmopause region (densities from 1 to 10 cm<sup>-3</sup>).

No major distinctions are made here between dayside and nightside. It appears, however, that the densities in the plasmopause region are slightly higher on the dayside, which will bias statistical studies of morphology. The plasma "trough" between the dayside plasmopause and magnetosheath is a poorly sampled region from the RIMS perspective, but it should be similar in behavior to the outer plasmopause region.

Further out along the (nightside) equator, in the plasma sheet proper, the observed portion of the core plasma is typically warm (temperatures of tens of electron volts or higher), and well measured. Such measurements are often (but not always) in reasonable agreement with densities inferred from plasma wave data. Given the experience in the plasmopause region, it would be wise to refrain from assuming that cold plasma does not exist in the plasma sheet, simply because it has not been observed.

At higher latitudes, above the ionosphere, densities are typically quite low. The field-aligned flows of the polar wind are observable up to a few thousand kilometers altitude, and then fade from view. At higher altitudes, these flows reappear, reported from ISEE-1 at geocentric distances up to 23 RE (Sharp et al., 1981). It is apparent that there is an acceleration region which is largely being missed, both spatially and energetically. This corresponds to the open regions of the detector simulations in figures 5 and 6.

## Conclusion

Core plasma measurements outside the plasmasphere proper are obscured by satellite charging effects. The measured plasma is distorted by charging effects, so that aspects of the plasma distribution (e.g. heat flux) may be incorrectly calculated. At altitudes greater than 25,000 km, the core plasma is often hidden due to charging effects. The polar wind

fades from view above 5,000 km, for many of the possible density/flow parameters. Proper interpretation of such measurements greatly depends on effective means of obtaining either density or potential independently, though the model described in this document can be used to reduce the uncertainty in density calculations from ion data. Complete measurement of the ambient plasma distribution will require effective means of satellite potential control.

## APPENDIX

Table 2 gives the times for the Spring, 1982 eclipses. Aperture bias settings and modes are noted, along with the plasma characteristics at eclipse entry and exit. If there is a reasonably sharp plasmopause during the eclipse, that is noted. If there are equatorially trapped ions during the eclipse, that is also noted. Density profiles for most of these time periods have been obtained from the plasma wave instrument, and have been noted.

### Glossary

- EN: Eclipse entry
- EX: Eclipse exit
- PP: Plasmopause
- EQ: Encountered equatorially trapped plasma
- Psheet: Plasma sheet – defined as observations of little or no isotropic plasma, with field-aligned (or no) plasma. Typically, field-aligned ions are bidirectional.
- Psphere: Plasmasphere – defined as low temperature, isotropic plasma, rammed.
- Ppouse: Plasmopause (region) at eclipse entry or exit, defined as mixed, anisotropic plasma. During this period, mixtures of field-aligned and isotropic plasma, often with equatorially-trapped plasma mixed in.

- PWID: Plasma wave instrument density profile done.
- M2834: Mass scan data during this season were taken in a mode which toggled between H<sup>+</sup>/He<sup>+</sup> and the molecular mass range (masses 28–34 in the high mass channel). These data result in useful spin curves for H<sup>+</sup>/He<sup>+</sup>, but of course no RPA curves.
- 8V: During about 50% of the passes, the aperture plane was fixed at –8 V bias. This is so noted as "8V".
- SS04P: A particularly unfortunate version of the 8 V bias this mode, which only provided RPA analysis up to 8 V, with only H<sup>+</sup>/He<sup>+</sup>. The result is that most of these times show saturated spin curves, and no RPA analysis.
- 0/8 There are 6 passes where the detector is cycling between 0 and –8 V aperture bias once every minute.
- 0/2/4/8 There are 2 passes where the detector is cycling according to the pattern 0/–2/0/–4/0/–8/0 V bias, once per minute.



# DYNAMICS EXPLORER 1

## Spring 1982 Eclipses

DATE	DAY	TIMES	COMMENTS
13-Feb	44	1236-1249	No data No data
14-Feb	45	0211-0237 0900-0930 1549-1623 2238-2321	No data No data No data 0/2/4/8 EN:PP; Psheet, EQ; EX:Psheet
15-Feb	46	0528-0613 1218-1305 1908-1957	0/8 Psheet EN: PP; EQ; EX: Psheet EN: PP; EQ (also parallel); EX: Psheet
16-Feb	47	0157-0249 0847-0941 1537-1633 2228-2325	EN: Psphere; PP: 0225; EX: Psheet 8V; EN: Psphere; EX: Psheet 8V; EN: Psphere; EQ: 1600; EX: Psheet: PWID M2834; EN: Psphere; EX: Psphere; PWID
17-Feb	48	0518-0616 1207-1308 1858-2000	0/8; EN:Psphere; EX: Psheet EN:Psphere; EQ: 1216; EX: Psheet, PWID 8V; EN:Psheet; EX:Psheet
18-Feb	49	0148-0251 0838-0943 1527-1634 2218-2326	EN:PP/EQ; EX:Psheet, PWID 8V; Psheet 8V; EN:PP; EQ: 1555; EX:Psheet: PWID EN:Psphere; EQ/PP:2230; EX:Psheet: PWID
19-Feb	50	0509-0617 1159-1309 1849-2000	Psheet; EQ:0450-0510; PWID 8V; Psheet Psheet; EQ:1915-1925; PWI off
20-Feb	51	0140-0252 0830-0943 1520-1634 2211-2325	M2834 - but off? - no data EN:Psphere; PP:0847; EX:Psheet; no MSFC fiche 8V; EN:Psphere; EQ/PP: 1555; EX:Psheet EN:Psphere; EQ:2220; off 2222-2300; E:Psheet
21-Feb	52	0459-0612  1149-1303  1200 on 1842-1959	EN:Psphere; EX:Psheet; PWID - in Hidden ion paper 0V data till 1154 UT. EN:Psphere. no MSFC fiche 8V; saturated till PP:1210; EX:Psheet, PWID EN:Psphere; EQ: 1918; EX: Psphere; PWID. in equator paper

22-Feb	53	0133-0250 0821-0937 1513-1633 2205-2324	M2834; EN:Psphere; PP:015G-0200; EX:Psheet off 8V; EN:Psheet; EQ:1535:1540; EX:Psheet 8V - no data yet in house
23-Feb	54	0452-0610 1145-1306 1835-1957	off 0/8; EN:Psphere; EQ:1155-1225; PP:1200; EX:Psheet 8V; no data yet
24-Feb	55	0124-0243 0817-0939 1508-1630 2157-2321	off EN:PP/EQ; EX:Psheet 8V; EN:Psheet; EQ:1530-1600 8V; EN:Psphere (ram 0+); EQ:2220 (dens minimum); PP:2237 (trapped 0+?) EX: Psheet; PWID
25-Feb	56	0450-0611 1140-1302 1830-1953	off 0/8 data??, not in house 8V; EN:PP; EQ:1905-1910; EX:Psheet
26-Feb	57	0121-0243 0812-0935 1502-1625 2153-2316	EN:Psphere; PP:0157; EX:Psheet EN:PP/EQ; EX:Psheet; PWID 8V; EN:Psphere; PP:1535; EX:Psheet EN:Psphere; PP:2200; EQ:2210-2230; EX: Psheet, PWID
27-Feb	58	0444-0607 1134-1259 1825-1948	off 8V-SS04P; EN:Saturated; EX:Psheet 8V; EN:Psphere; EQ:1900-1925; PP:1937; EX Psheet: PWID
28-Feb	59	0116-0239 0806-0930 1457-1620 2148-2311	off EN:Psphere(PP); EX:Psheet(PP); PWID in Hidden ion article, EQ 0810 8V-SS04P - no data M2834; EN:Psphere; PP:2240; EX:Psheet
1-Mar	60	0439-0602 1128-1254 1820-1943	off M2834; EN:Psphere; PP:1224; EX:Psheet; PWID M2834; EN:Psheet; EX:Psheet
2-Mar	61	0111-0234 0802-0924 1453-1615 2142-2307	EN:Psheet/EQ: Data end @ 0137 off 8V; EN:Psheet; EQ:1540? 8V; Psheet
3-Mar	62	0434-0556 1125-1246 1815-1938	EN:Psphere/EQ(415-445); PP:0437; EX:Psheet off M2834; Unclear - Psphere?: EQ:1905

4-Mar	63	0107-0227 0757-0919  1448-1610 2139-2300	no data? EN:Psphere (N=100); EQ:0803; PP:0830 EX:Psheet; PWID 8V; EN:Psphere (ram 0+); EQ:1525-1600; EX:PP 8V; EN:Psphere (ram 0+); PP:2255; EX:PP
5-Mar	64	0430-0549 1121-1240 1812-1930	M2834 - data?? EN:Psphere; EQ:1155; PP:1230; EX:Psheet 8V-SS04P Saturated
6-Mar	65	0103-0221  0754-0911 1445-1602 2136-2251	8V; EN:Psphere (ram 0+); PP:0203; EX:Psheet good case for disappearance of parallel B ions at eclipse exit EN:Psphere (0+); EX:Psphere 8V- SS04P - Saturated EN:Psphere(N=400); EX:Psphere(N=100)
7-Mar	66	0427-0543 1117-1233  1809-1922	M2834; EN:Psphere; PP:0515; EX:Psheet EN:Psphere(n=400); EQ:1152; EX:Psphere (n=70) PWID - in hidden ion article 8V-SS04P - Saturated
8-Mar	67	0100-0212 0750-0903 1442-1552 2133-2243	8V; no MSFC fiche, He+ sat. in GSFC fiche EN: Psphere(n=400); EX:Psphere(n=70), PWID 8V-SS04P - Saturated EN:Psphere; EQ/PP:2200; EX:Psheet, no MSFC fiche
9-Mar	68	0424-0534 1115-1224  1805-1914	EN:Psphere; PP:0450; EX:Psheet, no MSFC fiche 8V, mostly saturated EN:Psphere (ram 0+); EX:Psphere EN:Psphere (n=100); EX:? funny day; PWID
10-Mar	69	0057-0204 0748-0854 1439-1540 2131-2234	EN:Psphere; PP:0110; EX:Psheet M2834 - no data?? EN:Psphere (n=400); EX:Psphere, PWID 8V; EN:Psphere; EQ:2155; EX:Psphere
11-Mar	70	0422-0523 1113-1213 1804-1903	M2834; EN:Psphere EN:Psphere(n=500); EX:Psphere(n=100) EN:Psphere (some 0+); EQ:1845-1900; EX:Psphere
12-Mar	71	0056-0153  0747-0842  1438-1532 2130-2222	8V; EN:Psphere (ram 0+); EQ:0100-0120; EX:Psphere; PP:0157 EN:Psphere; PP:0815; EX:PP; PWID Good case for disappearing parallel B ions - PW? EN:Psphere (n=70); EX:PP(n=40)/EQ; PWID EN:Psphere (n=400); PP:2200-2205; EX:Psheet

13-Mar	72	0421-0510	EN:Psphere; PP:0445 (Parallel B 0+ appears!) EX:Psheet; PWID
		1113-1201	0/8; EN:Psphere; EX:Psheet
		1805-1850	8V; EN:Psphere; EQ:1845; EX:Psphere; PWID
14-Mar	73	0056-0139	EN:Psphere; EX:Psphere(?); PWID
		0747-0828	0/8; EN:Psphere; EX:Psphere, PWID
		1440-1517	0/2/4/8; EN:Psphere; EQ:1525;PWID
		2131-2206	EN:Psphere; EQ:2145-2155; EX:PP; PWID
15-Mar	74	0423-0455	0/2/4/8; EN:Psphere; EX:Psphere
		1117-1143	8V; Psphere, mostly saturated
		1810-1831	8V; EN:Psphere; PP:1820; EX:PP
16-Mar	75	0104-0118	Psphere

## BIBLIOGRAPHY

- Banks, P. M. and T. E. Holzer, The Polar Wind, J. Geophys Res., 73, 6846, 1968.
- Chappell, C. R., J. L. Green, J. F. E. Johnson, and J. H. Waite, Jr., Pitch angle variations in magnetospheric plasma – Initial observations from Dynamics Explorer 1, Geophys. Res Lett., 9, 933–936, 1982.
- Comfort, R. H., J. H. Waite, and C. R. Chappell, Thermal ion temperatures from the retarding ion mass spectrometer on DE-1, J. Geophys., 90, 3475–3486, 1985.
- Craven, P. D., R. C. Olsen, J. Fennell, D. Croley, T. Aggson, Potential modulation on the SCATHA spacecraft. J. Spacecraft & Rockets. 24, 150–157, 1987.
- Decreau, P.M.E., D. Carpenter, C.R. Chappell, R. H. Comfort, J. L. Green, R. C. Olsen, and J. H. Waite. Latitudinal plasma distribution in the dusk plasmaspheric bulge: Refilling phase and quasi-equilibrium state, J. Geophys Res., 86, 6929–6943, 1986.
- Gallagher, D. L., J. D. Menietti, J. L. Burch, A. M. Persoon, J. H. Waite, and C. R. Chappell. Evidence of high densities and ion outflows in the polar cap during the recovery phase. J. Geophys. Res., 91, 3321–3327, 1986.
- Gussenhoven, M. S., D. A. Hardy, F. Rich, W. J. Burke, and H. C. Yeh. High-level spacecraft charging in the low altitude polar auroral environment, J. Geophys Res., 90, 11009–11023, 1985.

Knott, K., P. Decreau, A. Korth, A. Pedersen, and G. Wrenn, Observations of the GEOS equilibrium potential and its relation to the ambient electron energy distribution, Proceedings of the 17th ESLAB Symposium of Spacecraft/Environment Interactions and their influence on Field and Particle Measurements, ESA SP-198, 1983.

Menietti, J. D., J. D. Winningham, J. L. Burch, W. K. Peterson, J. H. Waite, and D. R. Weimer, Enhanced ion outflows measured by the DE 1 high-altitude plasma instrument in the dayside plasmasphere during the recovery phase, J. Geophys. Res., 90, 1653-1668, 1985.

Nagai, T., J. F. E. Johnson, and C. R. Chappell, Low Energy ion pitch angle distributions in the magnetosphere by ISEE-1, J. Geophys. Res., 88, 6944-6960, 1983.

Nagai, T., J. H. Waite, J. L. Green, C. R. Chappell, R. C. Olsen, and R. H. Comfort, First measurements of supersonic polar wind in the polar magnetosphere, Geophys. Res. Lett., 11, 669-672, 1984.

Olsen, R. C., Field-aligned ion streams in the earth's midnight region, J. Geophys. Res., 87, 2301-2310, 1982.

Olsen, R. C., and C. K. Purvis, Observations of charging dynamics, J. Geophys. Res., 88, 5657-5667, 1983.

Olsen, R. C., R. H. Comfort, M. O. Chandler, T. E. Moore, J. H. Waite, D. L. Reasoner, and A. P. Biddle, DE 1 RIMS operational characteristics, NASA TM 86527, October, 1985a.

Olsen, R. C., C. R. Chappell, D. L. Gallagher, J. L. Green, D. A. Gurnett, The hidden ion population – Revisited, J. Geophys. Res., 90, 12121–12132, 1985b.

Olsen, R. C., C. R. Chappell, and J. L. Burch, Aperture plane potential control for thermal ion measurements, J. Geophys. Res., 91, 3117–3129, 1986.

Olsen, R. C., S. D. Shawhan, D. L. Gallagher, J. L. Green, C. R. Chappell, and R. R. Anderson, Plasma observations at the earth's magnetic equator, J. Geophys. Res., 92, 2385–2407, 1987.

Olsen, R. C., The record charging events of ATS-6, J. Spacecraft Rockets, 24, 362–366, 1987.

Schmidt, R. and A. Pedersen, Long-term behavior of phot electron emission from the electric field double probe sensors on GEOS-2, Planet. Space Sci., 35, 61–70, 1987.

Sharp, R. D., D. L. Carr, W. K. Peterson, and E. G. Shelley, Ion streams in the magnetotail, J. Geophys. Res., 86, 4639–4648, 1981.

Sojka, J. J., R. W. Schunk, J. F. E. Johnson, J. H. Waite, and C. R. Chappell, Characteristics of thermal and suprathermal ions associated with the dayside plasma trough as measured by the Dynamics Explorer retarding ion mass spectrometer, J. Geophys. Res., 88, 7895–7911, 1983.

## FIGURES

Figure 1. DE-1 RIMS density potential relationship. Density is the H<sup>+</sup> density obtained from the thin-sheath analysis algorithm developed by Comfort. The satellite potential is a by-product of that analysis, and is obtained self-consistently. The H<sup>+</sup> density will ordinarily be about 80% of the total density in this region. AM data are plotted with dots, PM data with plus (+) signs.

Figure 2. GEOS density potential relationship, with RIMS data superimposed. The reference to Knott et al., 1984 is taken from the Schmidt and Pedersen (1987) figure. The reference should apparently be to Knott et al., 1983.

Figure 3. Simulated RIMS response to core plasma (isotropic H<sup>+</sup> Maxwellians) for various densities. Satellite potential is obtained from Figure 2. Temperature is 1.0 eV. (a) end head (z) RPA response (b) radial detector spin curves.

Figure 4. Radial detector flux (count rate) as a function of density, with parameter temperature varying from 0.1 to 1.0 eV. (a) Apogee, Satellite Velocity 2.5 km/s, (b) 2.7 RE Geocentric, 5 km/s (c) 1.5 RE Geocentric., 7.5 km/s.

Figure 5. DE/RIMS polar wind response, as a function of altitude. Ionosphere flux =  $2 \times 10^8$  ions/cm<sup>2</sup>s. (a) 1 RE along B (b) 2 RE along B (c) 3 RE along B (d) apogee.

Figure 6. DE/RIMS polar wind response. Distance along B is 3 RE for a, b, c.



Figure 7. Spin-time spectrograms for an eclipse passage, day 47 of 1982.  $H^+$  and  $He^+$  are plotted. Eclipse entry is at 2225 UT, exit at 2327 UT. Flux (count rate) is plotted with a line shading technique – higher density of lines corresponds to higher flux.

Figure 8. Spin time ( $He^+$ ) and RPA time ( $H^+$  &  $He^+$ ) spectrograms for an eclipse passage, day 65 of 1982. The first 4 minutes of the RPA data are not useful, due to the absence of a "memory load." It is during this time segment that the satellite enters eclipse, at 0752. Eclipse exit is at 0910 UT.

Figure 9. Spin time and RPA time spectrograms for  $H^+$  on day 46 of 1982. Eclipse entry is at 1907 UT. The equator crossing at 1928 UT reveals equatorially trapped plasma (enhanced fluxes at  $90^\circ$  pitch angle, higher flux, or at least up to higher RPA voltages in the end head). The warm background fades at eclipse exit, 1952 UT.

Figure 10. Orbit plot for day 287 of 1981.

Figure 11. Spin time spectrograms – day 287, 1981,  $H^+$ , a) 0V bias, b)  $-2$  V bias, c)  $-4$  V bias, d)  $-8$  V bias. RPA settings from zero to one volt are included.

Figure 12. As in figure 11, but for  $He^+$ .

Figure 13. RPA time spectrograms for  $H^+$ , as in Figure 11. All spin phases are included (averaged).

Figure 14. Barrier effect. The top segment illustrates how potential varies in height above a biased set of conductors. The bottom segment shows the variation in potential along the plane of the conductors.

Figure 15. Spectrograms for 23 Oct 1983 (day 296) at 0V bias and -8V bias. H<sup>+</sup> and He<sup>+</sup> data are shown. Spin time spectrograms are for (effectively) zero vote RPA. The +Z RPA time plots average over all spin phase angles. The count rate scale for plot (f), the H<sup>+</sup> spin time plot, utilizes the flux scale in the lower right hand corner. The remaining plots are with the upper flux (count rate) scale.

Figure 16. H<sup>+</sup> count rate during aperture bias cycling, shows channeltron degradation effect. Bias sequence is 0/-2/0/-4/0/-8. Data are from the radial detector.

Figure 17. He<sup>+</sup> counts. as in Figure 16.

Figure 18. Summary diagram of DE/RIMS charging studies.

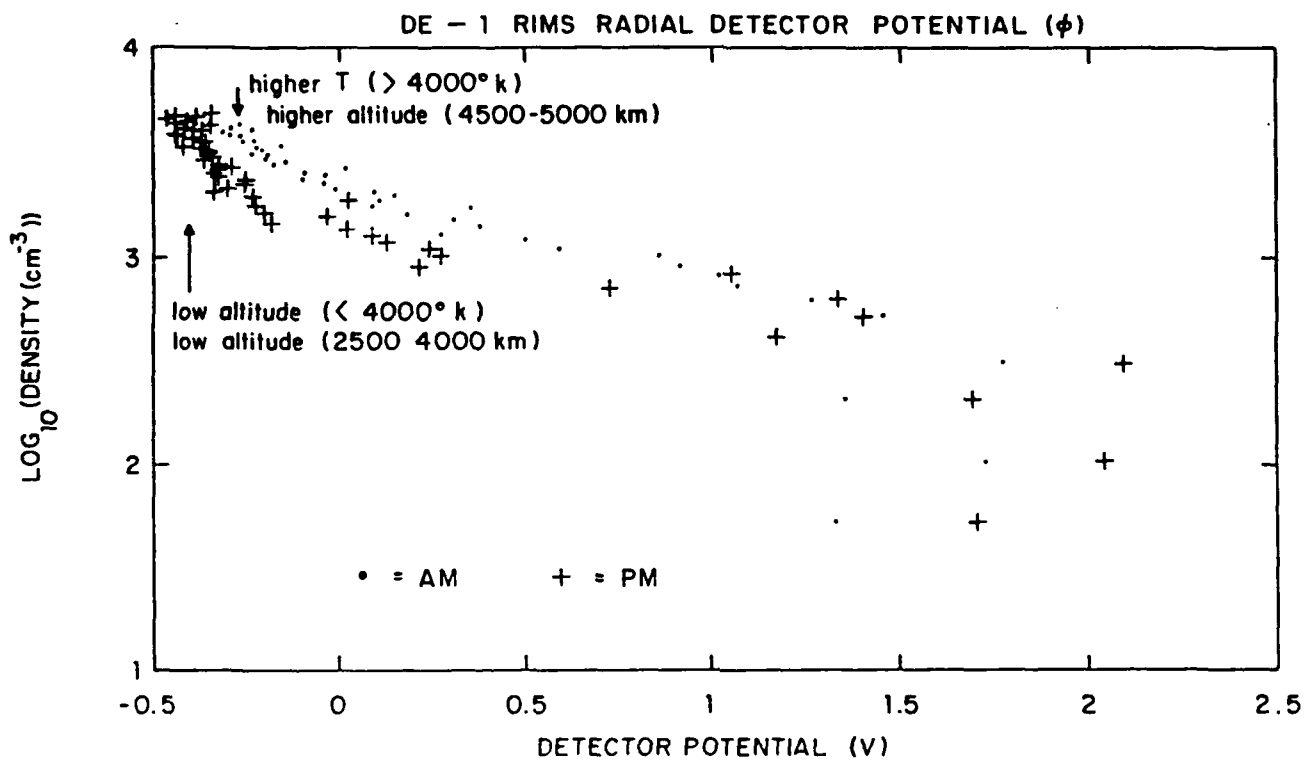


Figure 1  
32

# DENSITY POTENTIAL RELATIONSHIP

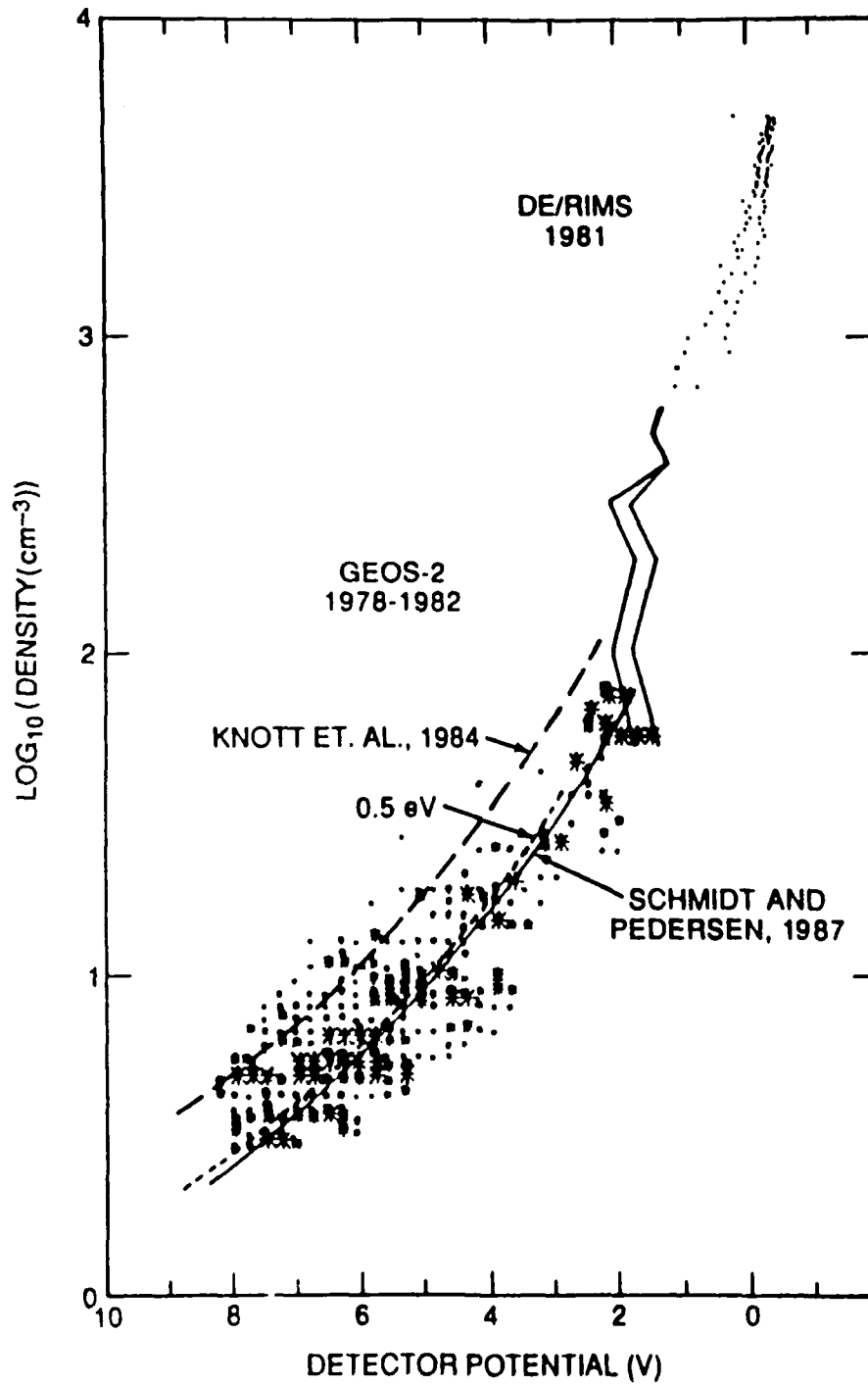
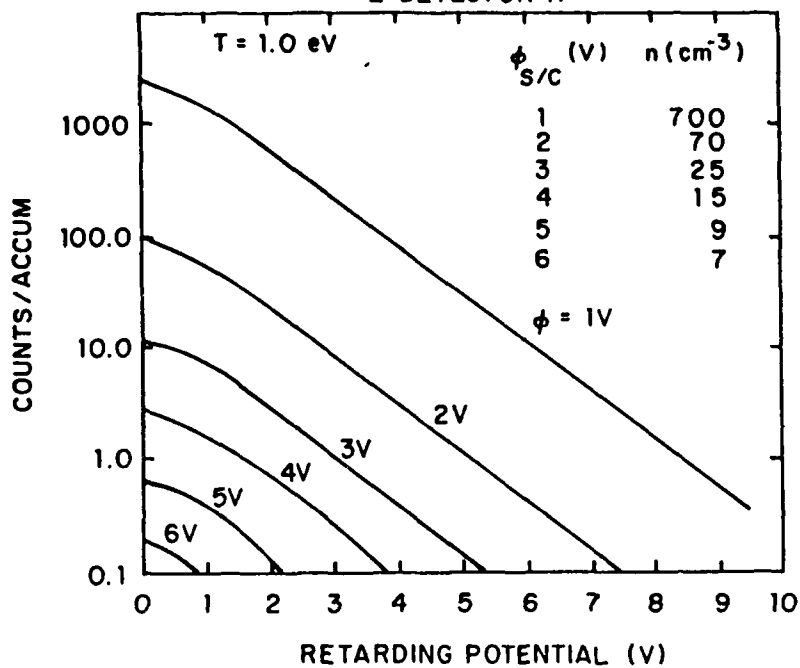


Figure 2

SIMULATED RIMS RESPONSE

Z DETECTOR H<sup>+</sup>



SIMULATED SPIN CURVES

RADIAL DETECTOR H<sup>+</sup>  
"CORE PLASMA"

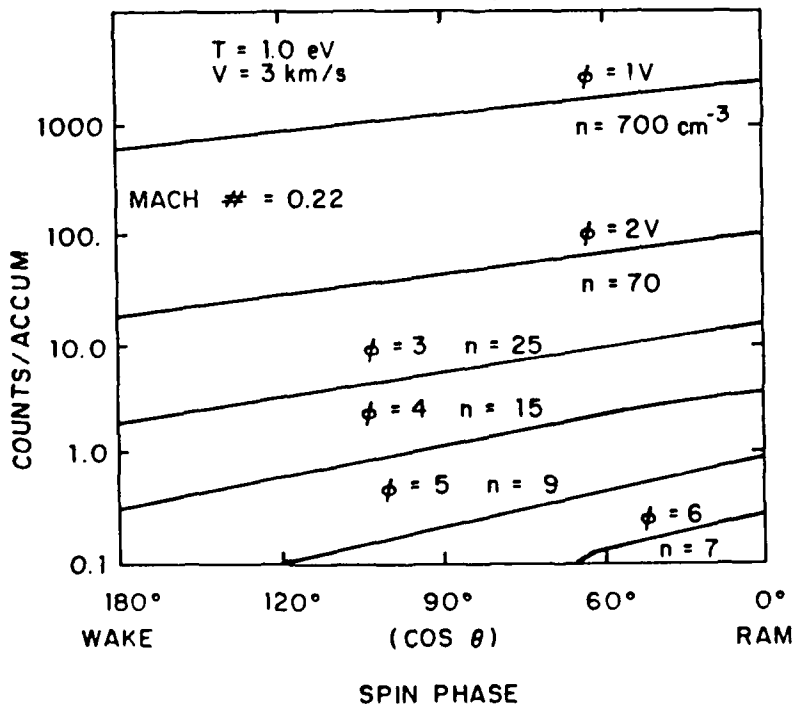


Figure 3

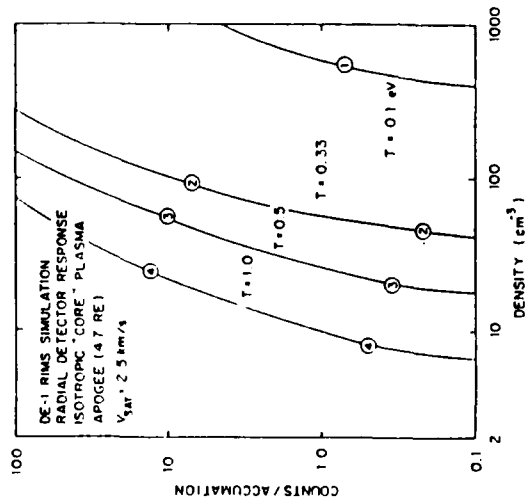
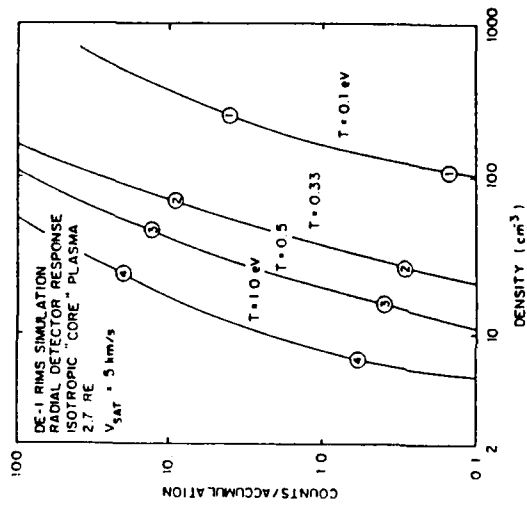
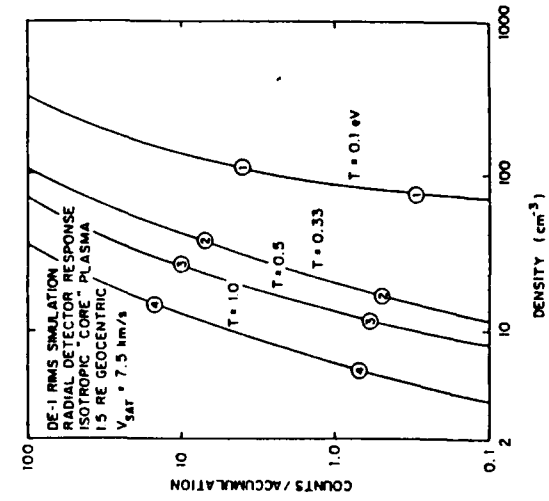


Figure 4

# DE-1 RIMS POLAR WIND RESPONSE

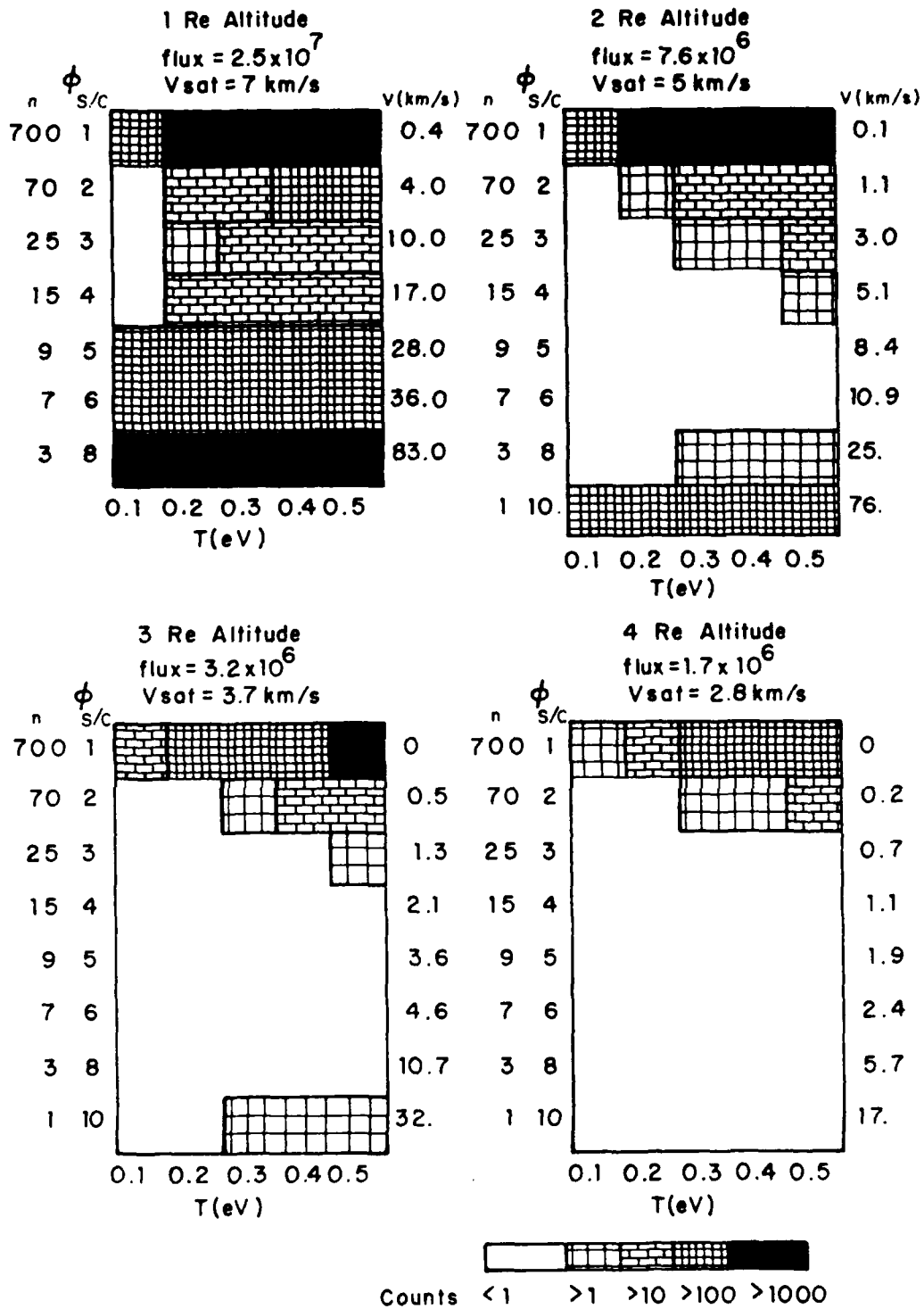


Figure 5

# DE-1 RIMS POLAR WIND RESPONSE

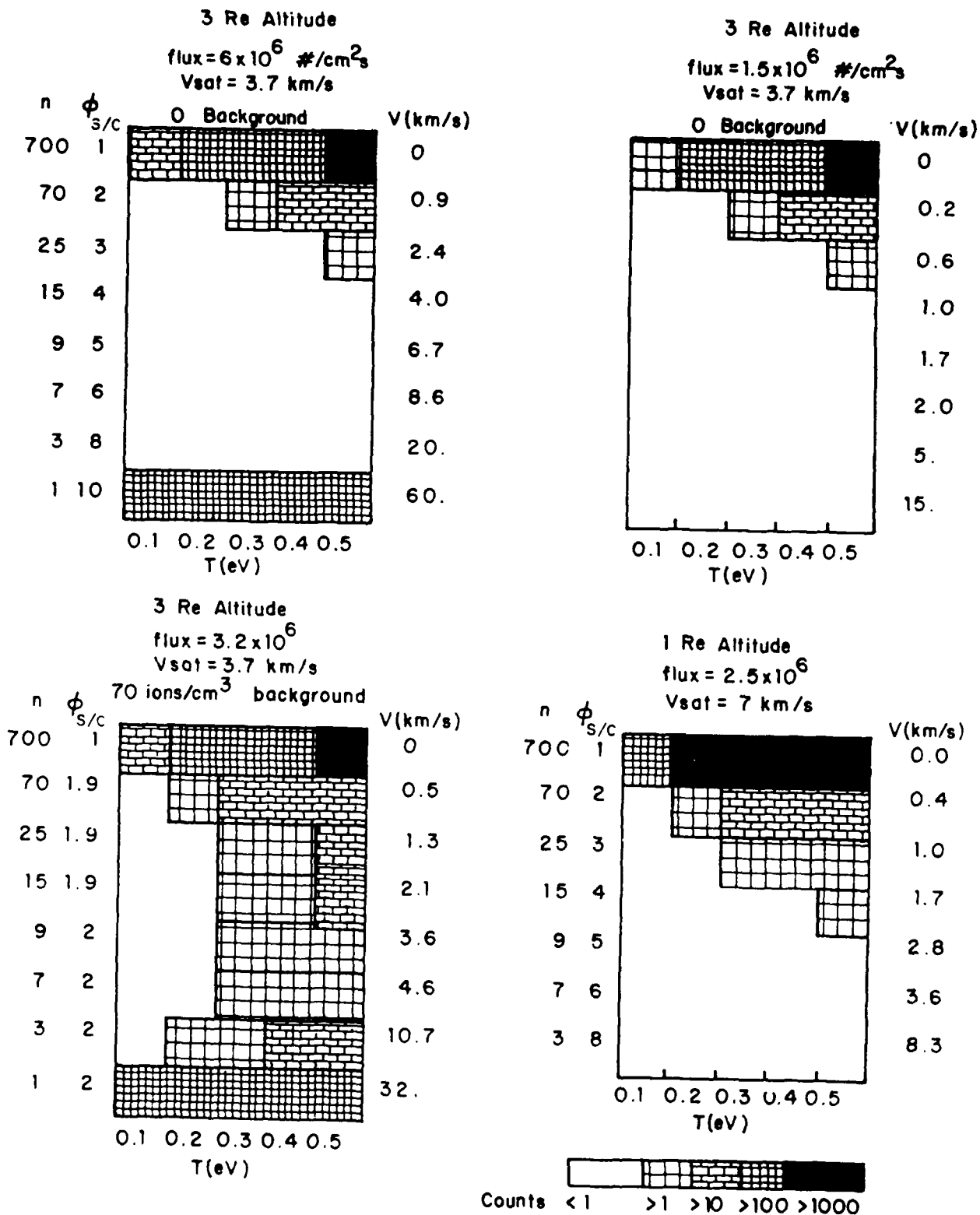


Figure 6



Dynamics Explorer I  
Retarding Ion Mass Spectrometer  
16 February 1982  
Radial Detector

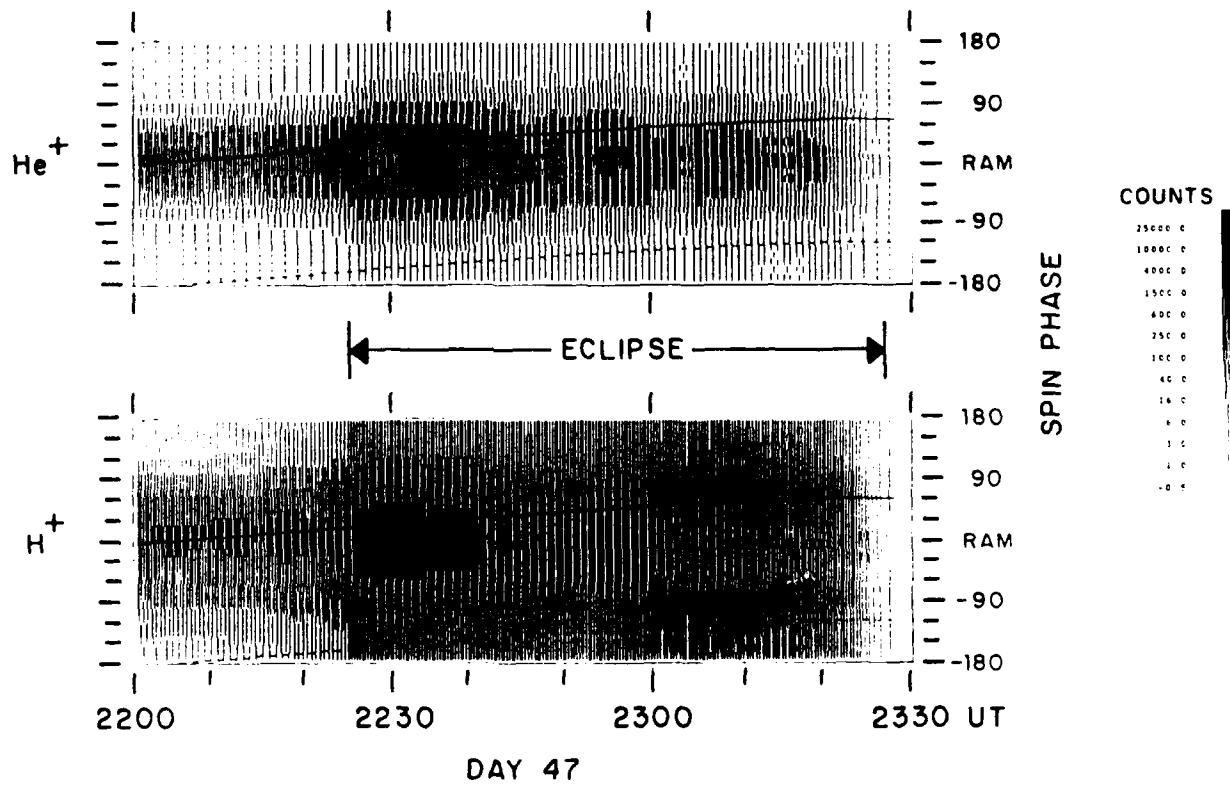


Figure 7

Dynamics Explorer I  
Retarding Ion Mass Spectrometer  
6 March 1982

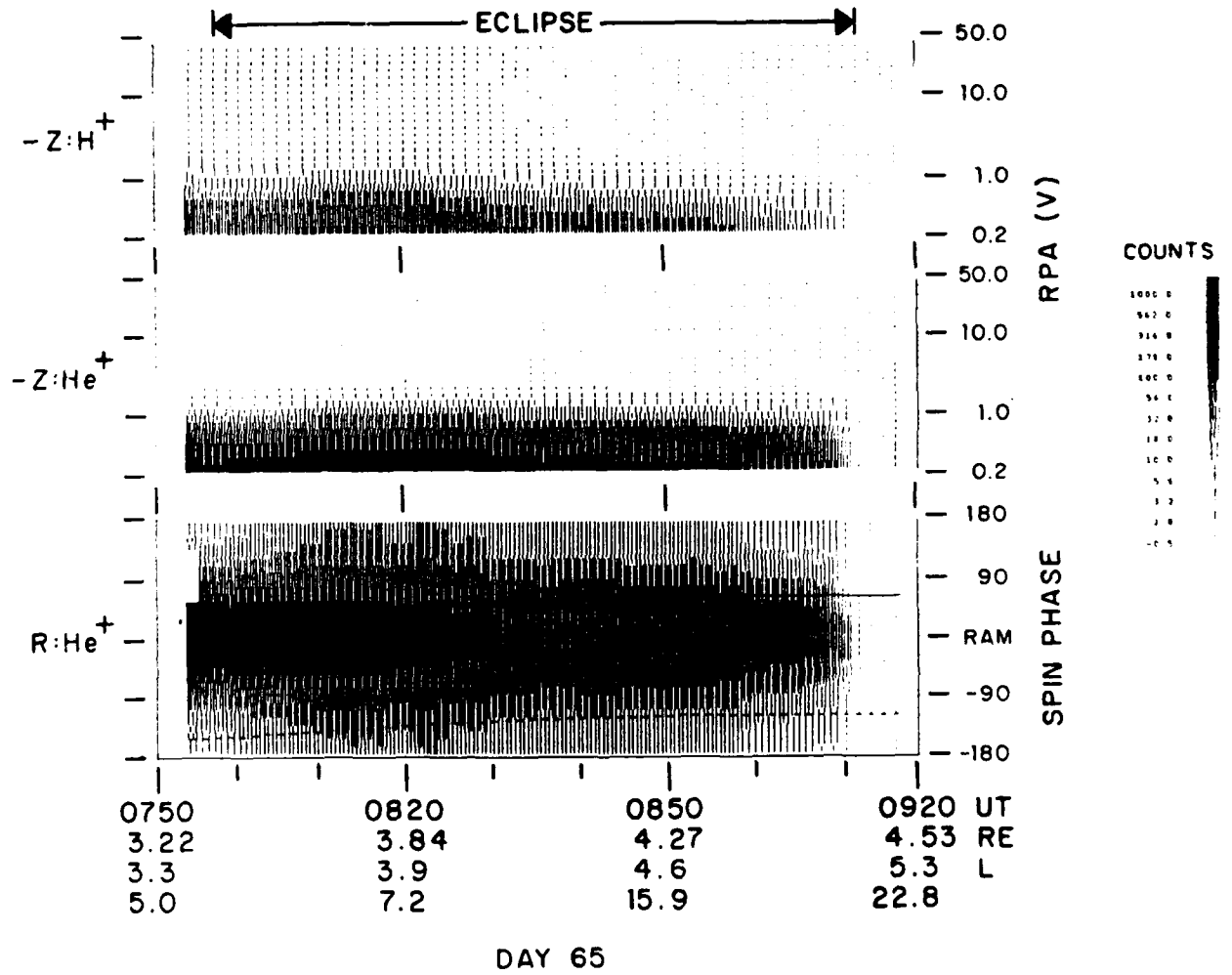


Figure 8

DE-1 RIMS  
15 February 1982

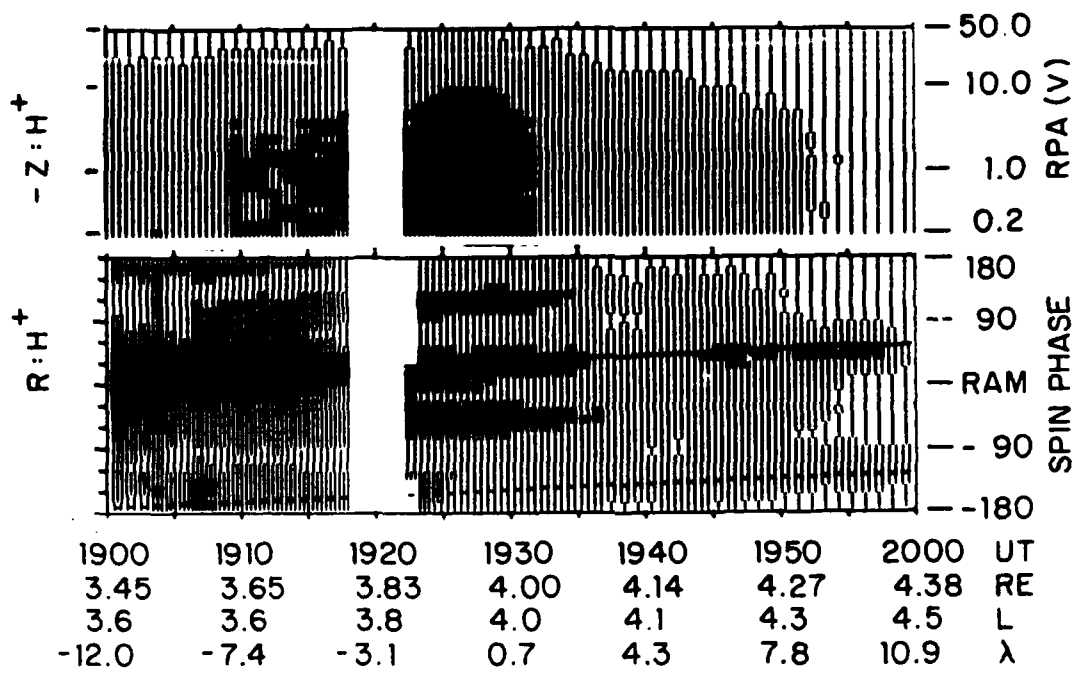


Figure 9

DYNAMICS EXPLORER I  
OCTOBER 14, 1981

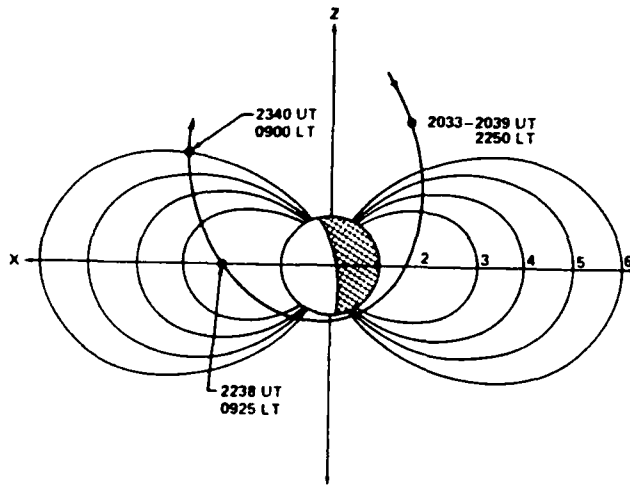


Figure 10

Dynamics Explorer I  
 Retarding Ion Mass Spectrometer  
 14-15 October 1981  
 Radial Detector - H<sup>+</sup>  
 0-1 V RPA

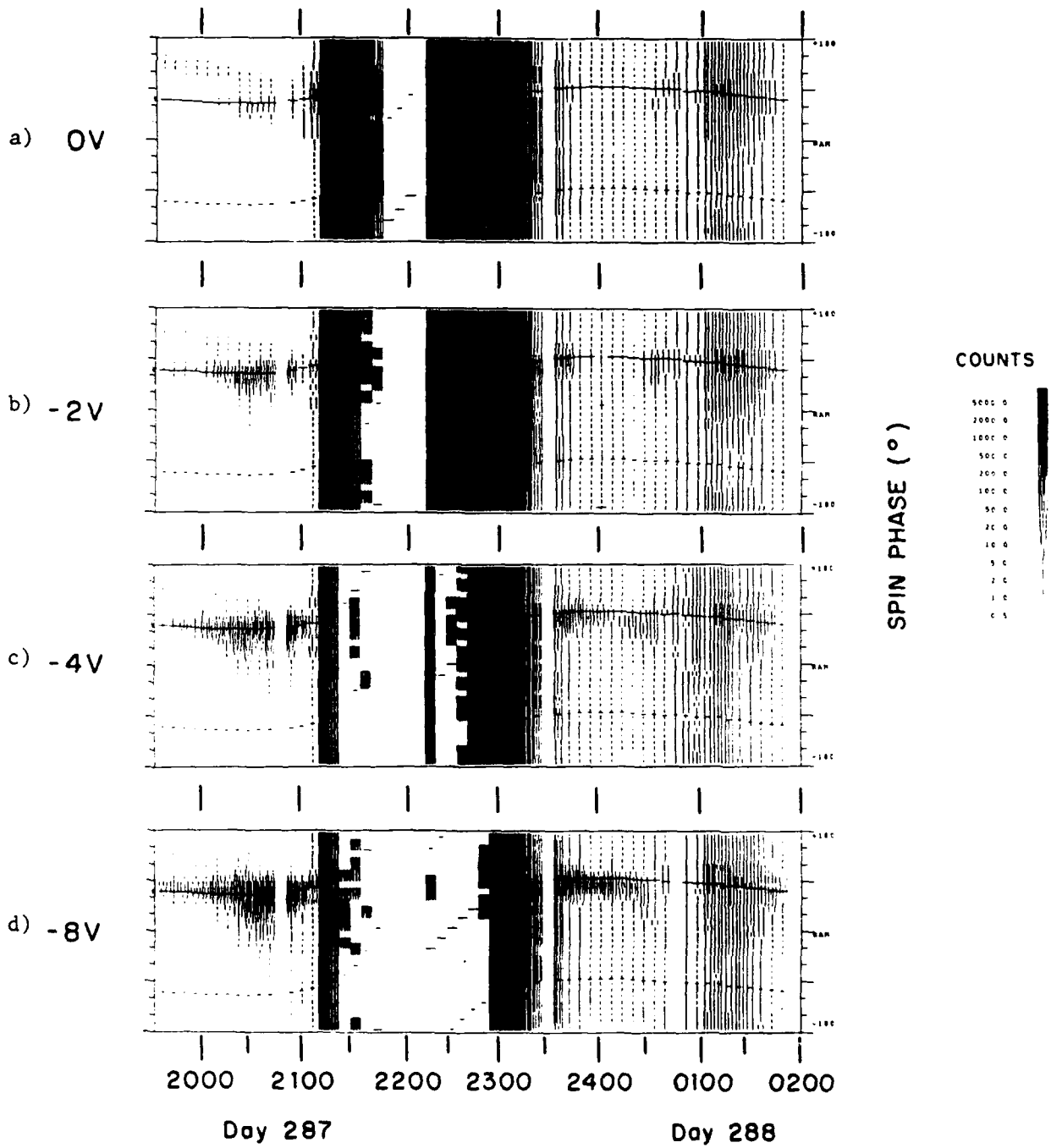


Figure 11

Dynamics Explorer I  
 Retarding Ion Mass Spectrometer  
 14 - 15 October 1981  
 Radial Detector - He<sup>+</sup>  
 0-1 V RPA

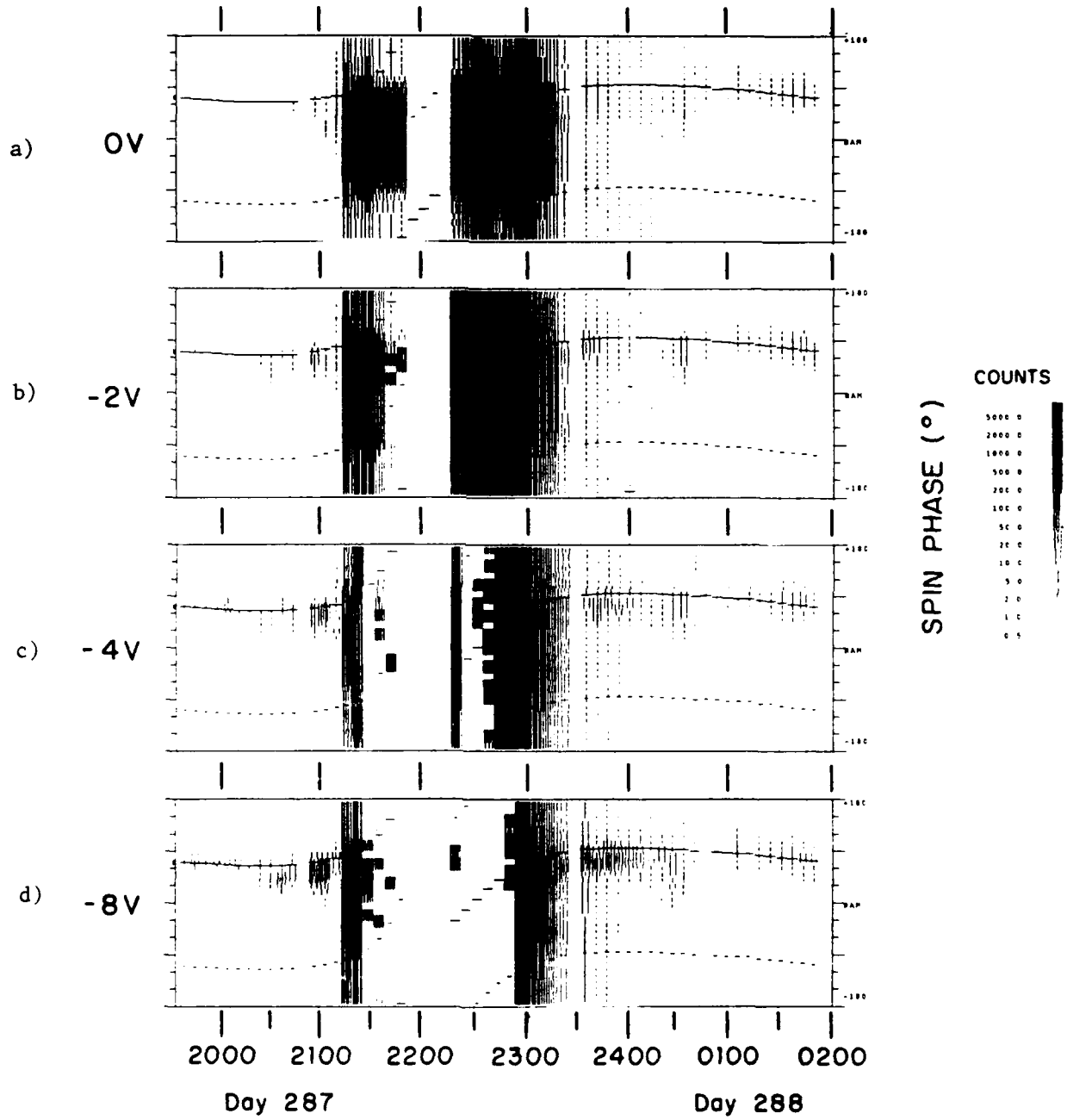


Figure 12

Dynamics Explorer I  
 Retarding Ion Mass Spectrometer  
 14-15 October 1981  
 Radial Detector - H<sup>+</sup>  
 All Spin Phase

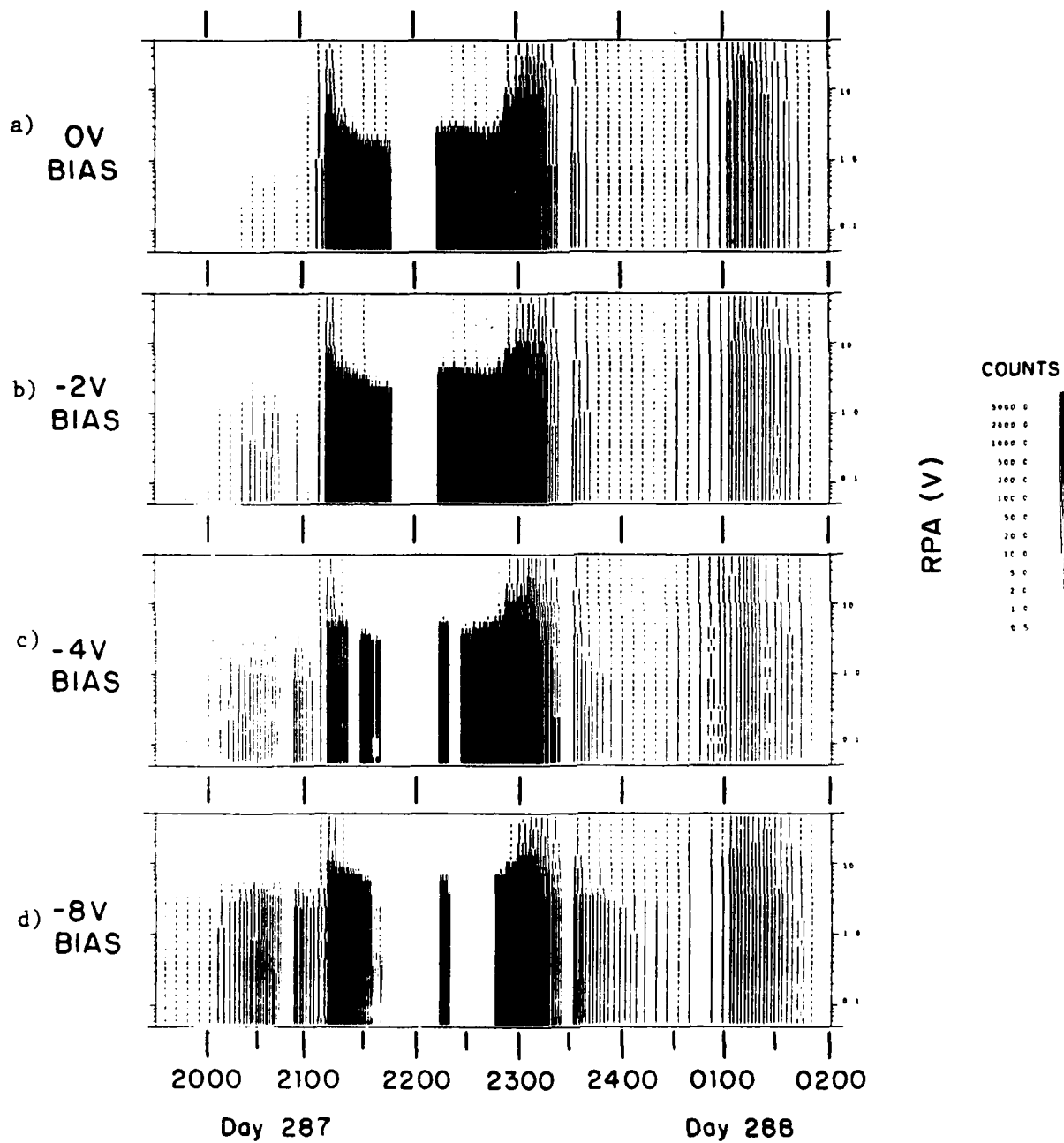


Figure 13

# Barrier Effect

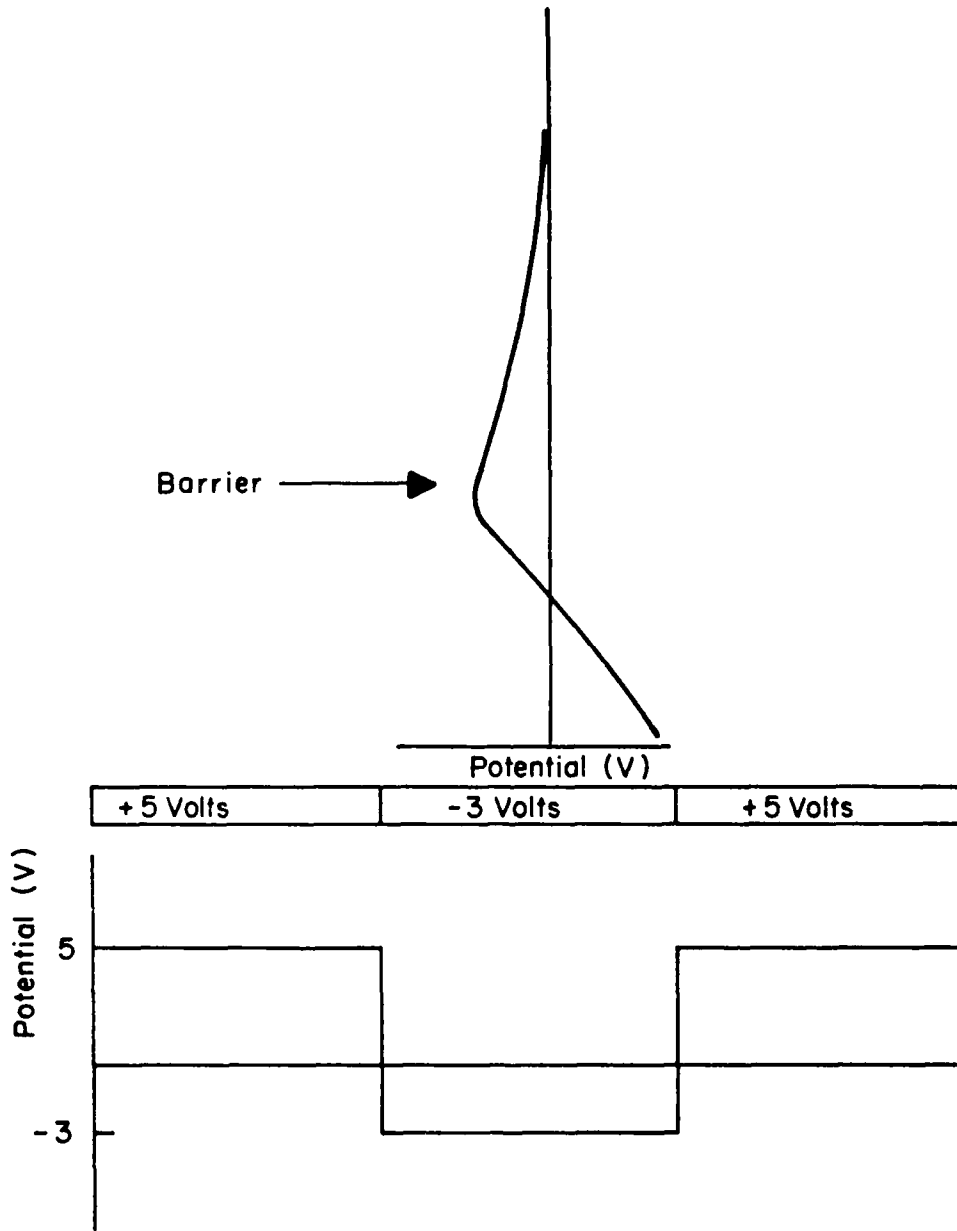


Figure 14



Dynamics Explorer I  
Retarding Ion Mass Spectrometer  
23 October 1983

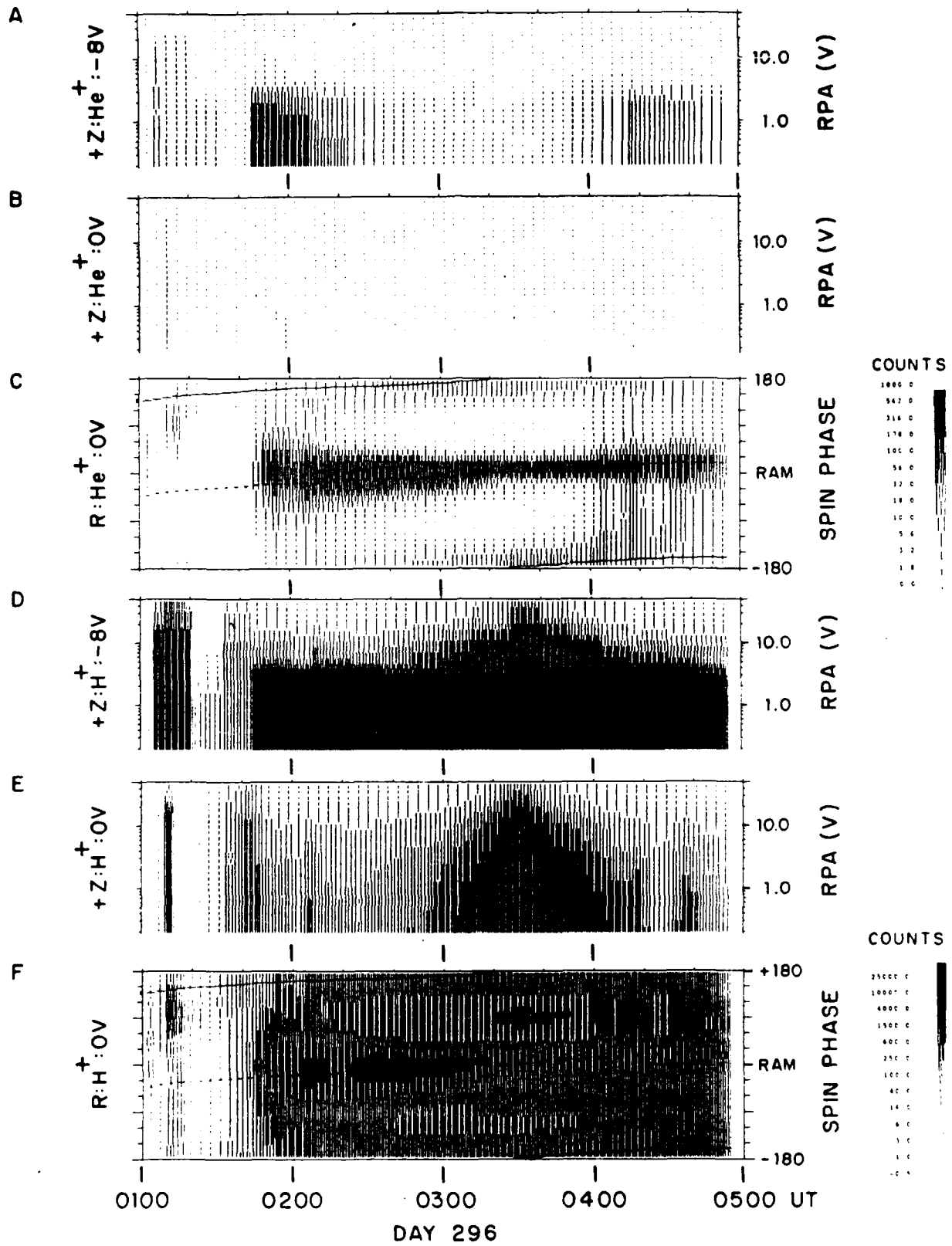


Figure 15

DE-1 RIMS  
16 MAY 1986 0857-0915 UT  
H<sup>+</sup> RPA: 0-1 Volt SPIN PHASE: ALL

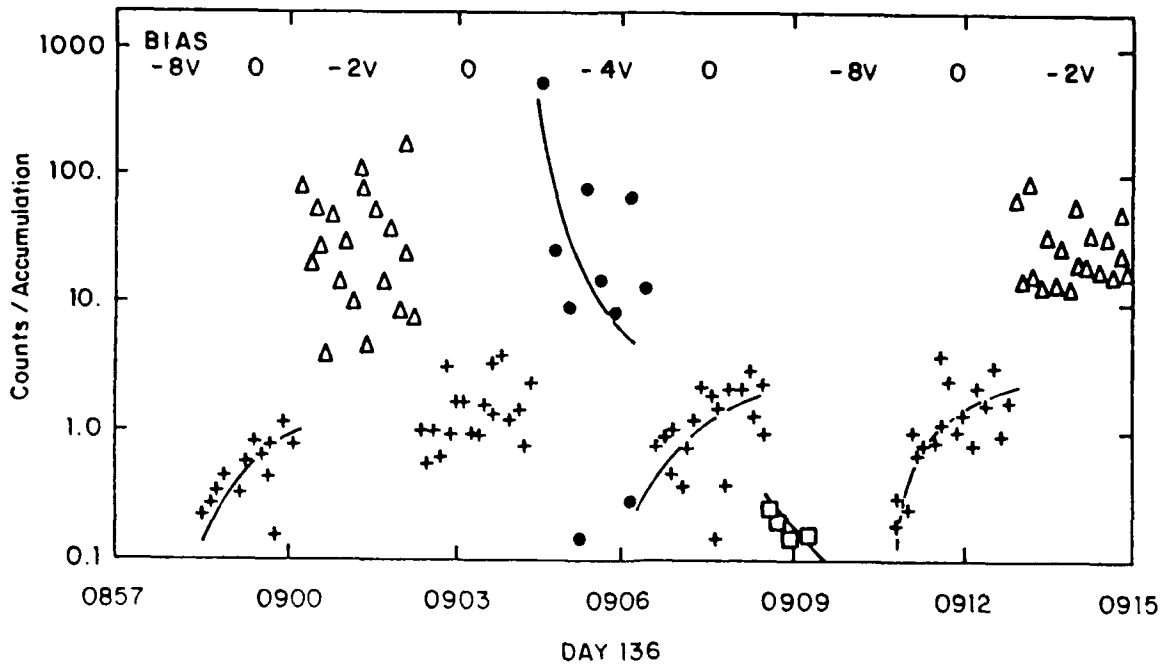


Figure 16

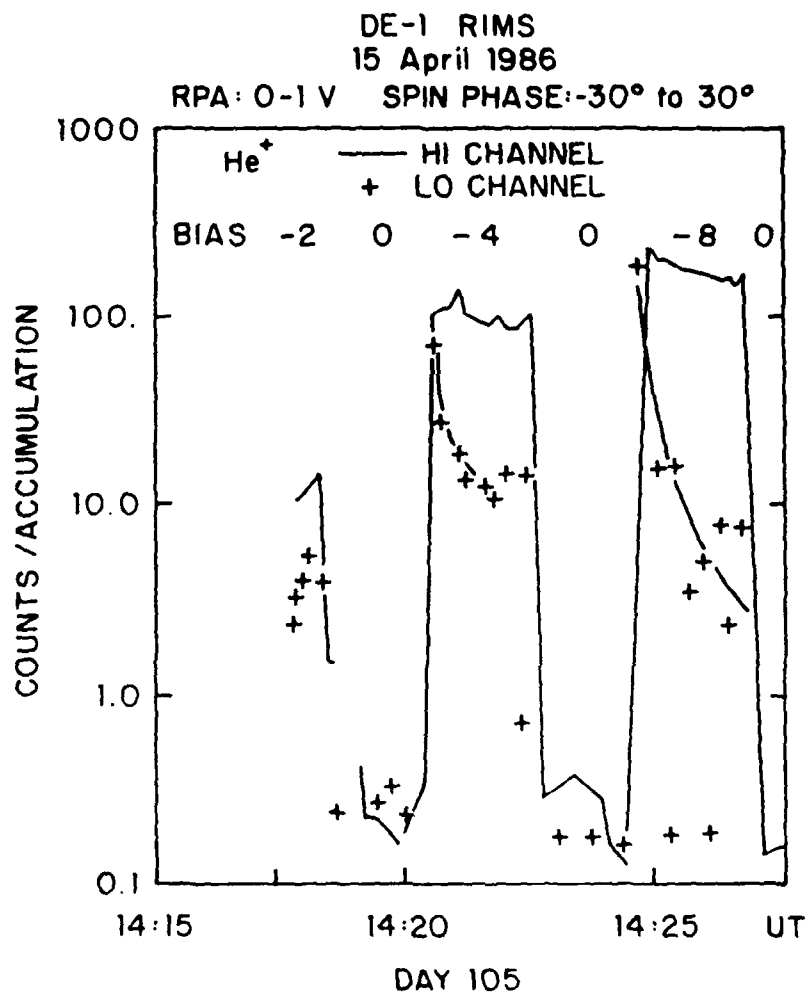
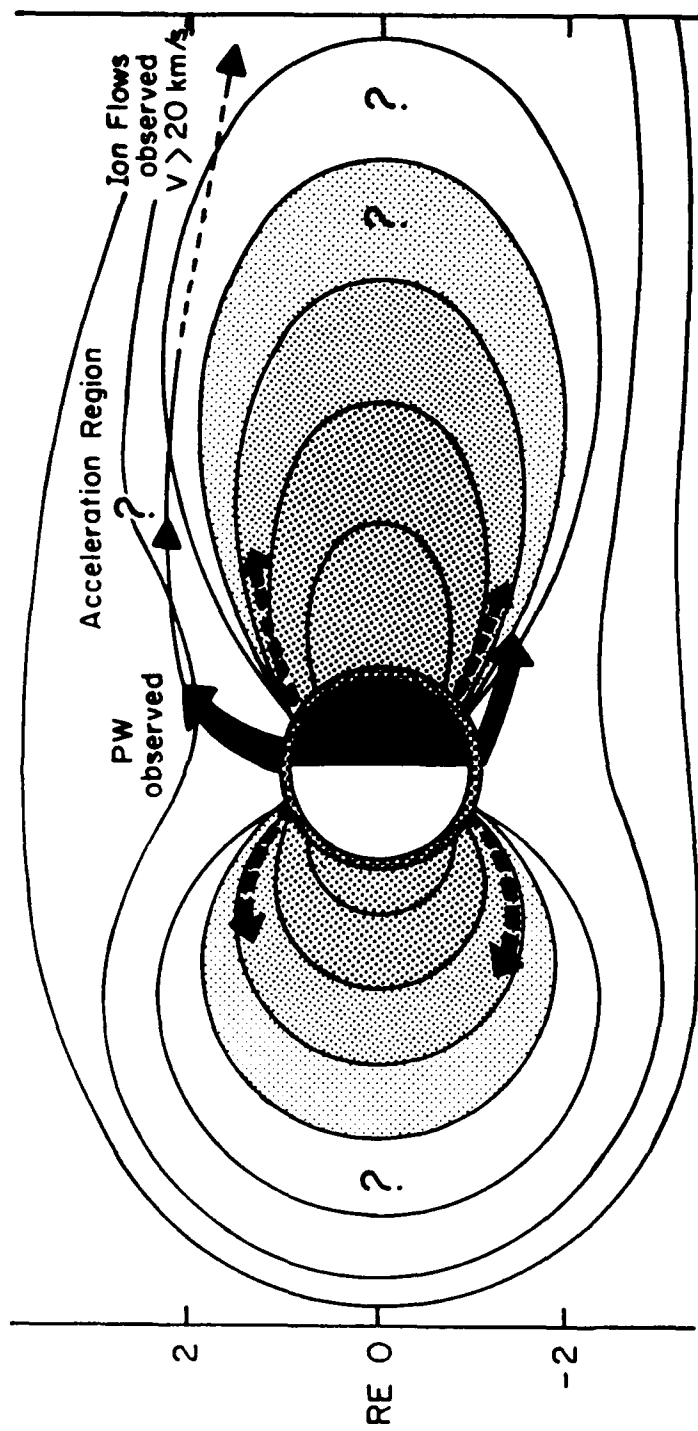


Figure 17

# MAGNETOSPHERE AND THERMAL PLASMA





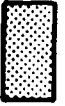



-  Ionosphere  $\phi \sim 0$  V
-  Inner Plasmasphere  $\phi < 1$  V
-  Outer Plasmasphere  $1 < \phi < 2$  V
-  Plasmopause,  $2 < \phi < 5$  V
-  Plasma sheet, lobes  $5 < \phi$
-  Subauroral flows

Figure 18

## DISTRIBUTION LIST

1. Library 2  
Naval Postgraduate School  
Monterey, California 93943
2. Research Administration (Code 012) 1  
Naval Postgraduate School  
Monterey, California 93943
3. Defense Technical Information Center 2  
Cameron Station  
Alexandria, VA 22314
4. Dr. C. R. Chappell 2  
Code DS01  
NASA Marshall Space Flight Center  
Huntsville, AL 35812
5. Dr. T. E. Moore 5  
Code ES53  
NASA Marshall Space Flight Center  
Huntsville, AL 35812
6. Mr. Paul Craven 2  
Code ES53  
NASA Marshall Space Flight Center  
Huntsville, AL 35812
7. Dr. Craig Pollock 2  
Code ES53  
NASA Marshall Space Flight Center  
Huntsville, AL 35812
8. Dr. M. Chandler 2  
Code ES53  
NASA Marshall Space Flight Center  
Huntsville, AL 35812
9. Dr. D. L. Reasoner 1  
Code ES53  
NASA Marshall Space Flight Center  
Huntsville, AL 35812
10. Ms. B. Giles 1  
Code ES53  
NASA Marshall Space Flight Center  
Huntsville, AL 35812

- |     |  |    |
|-----|--|----|
| 11. | Ms. V. Coffey<br>Code ES53<br>NASA Marshall Space Flight Center<br>Huntsville, AL 35812                                | 1  |
| 12. | Dr. R. H. Comfort<br>CSPARA<br>University of Alabama<br>Huntsville, AL 35899   | 2  |
| 13. | Dr. J. L. Horwitz<br>CSPARA<br>University of Alabama<br>Huntsville, AL 35899   | 1  |
| 14. | Dr. G. R. Wilson<br>CSPARA<br>University of Alabama<br>Huntsville, AL 35899  | 1  |
| 15. | Dr. J. H. Waite<br>Southwest Research Institute<br>PO Drawer 28510<br>San Antonio, TX 78284                            | 1  |
| 16. | Dr. D. Young<br>Southwest Research Institute<br>PO Drawer 28510<br>San Antonio, TX 78284                               | 1  |
| 17. | Dr. E. C. Whipple<br>CASS<br>UCSD<br>La Jolla, CA 92093  | 1  |
| 18. | Dr. Andrew Yau<br>National Research Council<br>Herzberg Institute of Astrophysics<br>Ottawa<br>Ontario, Canada K1A 0R6 | 1  |
| 19. | Dr. R. C. Olsen<br>Code 610s<br>Naval Postgraduate School<br>Monterey, CA 93943  | 20 |